FRA-75-23

REPORT NO. FRA-OR&D-76-253

A STUDY OF LINEAR INDUCTION MOTOR CHARACTERISTICS: THE MOSEBACH MODEL

John J. Stickler

U.S. DEPARTMENT OF TRANSPORTATION
TRANSPORTATION SYSTEMS CENTER
Kendall Square
Cambridge MA 02142

MAY 1976

INTERIM REPORT

Prepared for

U.S. DEPARTMENT OF TRANSPORTATION
FEDERAL RAILROAD ADMINISTRATION
Research and Development
Washington DC 20590

NOTICE

This document is disseminated under the sponsorship of the Department of Transportation in the interest of information exchange. The United States Government assumes no liability for its contents or use thereof.

NOTICE

The United States Government does not endorse products or manufacturers. Trade or manufacturers' names appear herein solely because they are considered essential to the object of this report.

Technical Report Documentation Page

1. Report No.	2. Government Accession No.	3. Recipient's Catalog No.
FRA-OR&D-76-253		

4. Title and Subtitle	5. Report Date
A STUDY OF LINEAR INDUCTION MOTOR CHARACTERISTICS: THE MOSEBACH MODEL	May 1976
	6. Performing Organization Code
7. Author(s) John J. Stickler	8. Performing Organization Report No. DOT-TSC-FRA-75-23
9. Performing Organization Name and Address U.S. Department of Transportation Transportation Systems Center Kendall Square Cambridge MA 02142	10. Work Unit No. (TRAIS) RR630/R6351
	11. Contract or Grant No.
12. Sponsoring Agency Name and Address U.S. Department of Transportation Federal Railroad Administration Research and Development Washington DC 20590	13. Type of Report and Period Covered Interim Report Sept. 1974 - Feb. 1975
	14. Sponsoring Agency Code

15. Supplementary Notes

16. Abstract

This report covers the Mosebach theory of the double-sided linear induction motor, starting with the idealized model and accompanying assumptions, and ending with relations for thrust, airgap power, and motor efficiency. Solutions of the magnetic induction equation for the one- and two-dimensional LIM models are presented. The effect of the magnitude of the Fourier unit cell length and maximum harmonic order on computer accuracy is discussed in some detail.

The one-dimensional Mosebach model is applied to the analysis of the LIMRV & TLRV LIMs and the results compared with similar predictions based on the Elliott, Oberretl, and Yamamura computer models. The report concludes that the Mosebach theory is of particular value when applied to linear motors operating at high speeds and low slip-frequencies.

17. Key Words	18. Distribution Statement
Linear Induction Motor Edge-Effect End-Effect LIM Propulsion Characteristics	APPROVED FOR FEDERAL RAILROAD ADMINISTRATION ONLY. THIS DOCUMENT IS EXEMPTED FROM PUBLIC AVAILABILITY BECAUSE IT IS AN INTERNAL WORKING PAPER AND DOES NOT REPRESENT A COMPLETED PROJECT. TRANSMITTAL OF THIS DOCUMENT OUTSIDE THE FRA MUST HAVE THE PRIOR APPROVAL OF THE FEDERAL RAILROAD ADMINISTRATION, RESEARCH AND DEVELOPMENT, OFFICE OF PASSENGER SYSTEMS.

19. Security Classif. (of this report)	20. Security Classif. (of this page)	21. No. of Pages	22. Price
Unclassified	Unclassified	66	

Form DOT F 1700.7 (8-72) Reproduction of completed page authorized

PREFACE

This report discusses the Mosebach theory of linear induction motors and its application to the analysis of high-speed motors used in ground transportation systems. It comprises the final report in a three-part series devoted to a review of current LIM theories and a study of computer predictions based on these theories. The first two reports examined the Oberretl and Yamamura theories of linear induction motors. Each report has as its objective the comparison of the relative predictions given by each theory and an examination of their differences as they relate to the models used in each theory.

The author is pleased to acknowledge the following individuals for numerous discussion and helpful information: Mr. Matthew Guarino, Jr. of the U.S. Federal Railroad Administration, Dr. Clem Skalski of MITRE Corporation, Dr. David G. Elliott of the Jet Propulsion Laboratory, and Professor James Melcher of the Massachusetts Institute of Technology.

METRIC CONVERSION FACTORS

Approximate Conversions to Metric Measures

Symbol	When You Know	Multiply by	To Find	Symbol
	LENGTH			
in	inches	2.5	centimeters	cm
ft	feet	30	centimeters	cm
yd	yards	0.9	meters	m
mi	miles	1.6	kilometers	km
	AREA			
in^2	square inches	6.5	square centimeters	cm^2
ft^2	square feet	0.09	square meters	m^2
yd^2	square yards	0.8	square meters	m^2
mi^2	square miles	2.6	square kilometers	km^2
	acres	0.4	hectares	ha
	MASS (weight)			
oz	ounces	28	grams	g
lb	pounds	0.45	kilograms	kg
	short tons (2000 lb)	0.9	tonnes	t
	VOLUME			
tsp	teaspoons	5	milliliters	ml
Tbsp	tablespoons	15	milliliters	ml
fl oz	fluid ounces	30	milliliters	ml
c	cups	0.24	liters	l
pt	pints	0.47	liters	l
qt	quarts	0.95	liters	l
gal	gallons	3.8	liters	l
ft^3	cubic feet	0.03	cubic meters	m^3
yd^3	cubic yards	0.76	cubic meters	m^3
	TEMPERATURE (exact)			
°F	Fahrenheit temperature	5/9 (after subtracting 32)	Celsius temperature	°C

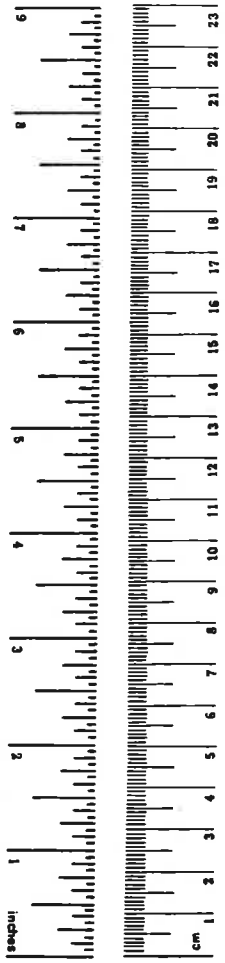

Approximate Conversions from Metric Measures

Symbol	When You Know	Multiply by	To Find	Symbol
	LENGTH			
mm	millimeters	0.04	inches	in
cm	centimeters	0.4	inches	in
m	meters	3.3	feet	ft
m	meters	1.1	yards	yd
km	kilometers	0.6	miles	mi
	AREA			
cm^2	square centimeters	0.16	square inches	in^2
m^2	square meters	1.2	square yards	yd^2
km^2	square kilometers	0.4	square miles	mi^2
ha	hectares (10,000 m^2)	2.5	acres	
	MASS (weight)			
g	grams	0.035	ounces	oz
kg	kilograms	2.2	pounds	lb
t	tonnes (1000 kg)	1.1	short tons	
	VOLUME			
ml	milliliters	0.03	fluid ounces	fl oz
l	liters	2.1	pints	pt
l	liters	1.06	quarts	qt
l	liters	0.26	gallons	gal
m^3	cubic meters	36	cubic feet	ft^3
m^3	cubic meters	1.3	cubic yards	yd^3
	TEMPERATURE (exact)			
°C	Celsius temperature	9/5 (then add 32)	Fahrenheit temperature	°F

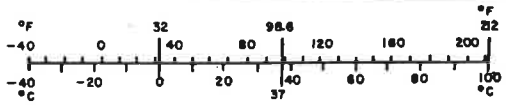

TABLE OF CONTENTS

LIST OF ILLUSTRATIONS

LIST OF ILLUSTRATIONS (CONTINUED)

LIST OF TABLES

LIST OF SYMBOLS

Symbol	
a_k	wave vector component along x direction
a_n	normalized Fourier coefficient of stator current sheet
A_z	stator current sheet
b	wave vector component along z direction
b_n^k	normalized Fourier coefficient of stator current sheet
B	magnetic flux density
B_n	complex Fourier coefficient of magnetic flux density
$\overline{B}$	matrix with Fourier coefficients of magnetic flux density
d_s	'sidebar' width of secondary
E_x	electric field along x direction
E_z	electric field along z direction
f	frequency
$f_k(x)$	parameter describing occupancy of stator slots of kth phase
F_x	total thrust (average)
G_x	secondary current density in x direction
G_z	secondary current density in z direction
I^k	exciting current of phase k
j	$\sqrt{-1}$
k	subscript denoting phase
K	primary surface current density
KP	ratio of expansion length to primary winding length
m	transverse harmonic order
n	longitudinal harmonic order
NMAX	maximum longitudinal harmonic order

Symbol	
P	number of poles
P_{ag}	air-gap power
P_m	mechanical power
P_{sec}	secondary power(loss)
q	number of slots in given phase belt
r	magnetic Reynolds number
r'	modified magnetic Reynolds number
R_1	stator phase resistance
R	matrix with effective Reynolds number in diagonal elements
s	slip
t	time
V	input phase voltage
x	longitudinal axis (direction of thrust)
X_1	primary leakage reactance
X_2	secondary leakage reactance
X_m	magnetizing reactance
y	axis normal to primary surface
y_1	half-thickness of secondary
y_2	half-width of core-to-core separation
y_{20}	half core-to-core separation within primary region
Y	matrix with Fourier coefficients of $y_2(x)$
z	transverse axis (direction of active primary current)
$Z^{kk'}$	elements of input impedance matrix
Z_{in}	input impedance of phase winding
Z_{ag}	air-gap phase impedance
σ	secondary conductivity
λ	sequence index

Symbol	
μ	sequence index
τ_p	pole pitch
ω	angular frequency

1. INTRODUCTION

This report examines the Mosebach theory of linear induction motors as outlined in the dissertation "Effekte der endlichen Läng and Breite bei asynchronen Linearmoteren in Kurzständer und Kurzläuferbauform" By H. Mosebach,[1] University of Braunschweig, Braunschweig, Germany. It is the third and final report in this series dealing with current linear induction motor (LIM) theories and their application to motor analysis. The first two reports, which discuss LIM treatments by K. Oberretl[2] and S. Yamamura,[3] describe two different approaches to the solution of the field equation of double-sided LIMs. Both treatments use LIM models with finite length primary excitations (MMF) but assume the primary iron to extend to infinity in the plane of the motor. Their solutions give predictions for LIM losses associated with the finite size of the primary but are unable to predict the additional losses arising from the finite size of the primary iron core. The Mosebach theory described in this report uses a LIM model having both finite MMF excitation and finite ferromagnetic primary. Its predictions should provide information on these additional losses and the effect which boundary related phenomena have on LIM performance.

The report is divided into two principle subject areas. The first describes the Mosebach theory and discusses various aspects of the model upon which it is based. The second applies the one-dimensional (Mosebach) computer program to predict the output characteristics of the Tracked-Levitated-Research-Vehicle (TLRV) and Linear-Induction-Research-Vehicle (LIMRV) motors. In the latter material, comparisons are given of the motor characteristics predicted by Mosebach (model) and those predicted by Yamamura, Oberretl, and Elliott (models).

2. TECHNICAL DISCUSSION

2.1 THE MOSEBACH MODEL

Because exact solutions of the field equations for actual LIMs are impossible, one must resort either to approximate solutions of real structures, or to exact solutions of idealized models of real structures. The Mosebach treatment takes the latter approach. It replaces the real motor, shown in Figure 1a, with an idealized model as illustrated in Figure 1b. The stator winding current is represented in the model by a surface current density sheet propagating in the x-direction. The secondary is described by a region with conductivity and dimensions equivalent to that of the real secondary.

The coordinates used in the model description are shown in Figure 1b. The origin is positioned at the center of the motor and inside the secondary. The secondary moves in the x-direction relative to the fixed primary. The y-axis denotes the direction normal to the motor surface and the z-axis denotes the direction along the transverse axis of the motor.

The LIM model simulates the fringing magnitude flux of the real motor by means of the linear gap function of 51 degrees shown in Figure 1b. In the idealized model, airgap flux is assumed to be restricted to the y-direction in the absence of secondary. Conformal mapping studies of the flux distribution of the real motor (comprising 90 degree air-iron interfaces at motor ends) without secondary reveal that the y-directed flux of the real motor is closely approximated by that of the idealized model at positions along the x-axis of the motor.[4]

Two versions of the above model are considered by Mosebach and referred to as the <u>one-dimensional LIM model</u> and the <u>two-dimensional LIM model</u>. The one-dimensional model treats the fringing fields at the motor ends only, by the use of the linear gap function. The ferromagnetic primary is assumed to be continuous in the transverse direction. The two-dimensional model uses the linear gap function to describe the varying magnetic

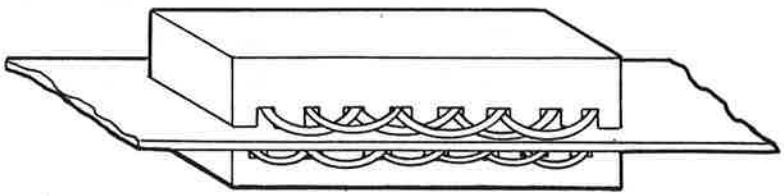

Figure 1a. Real LIM

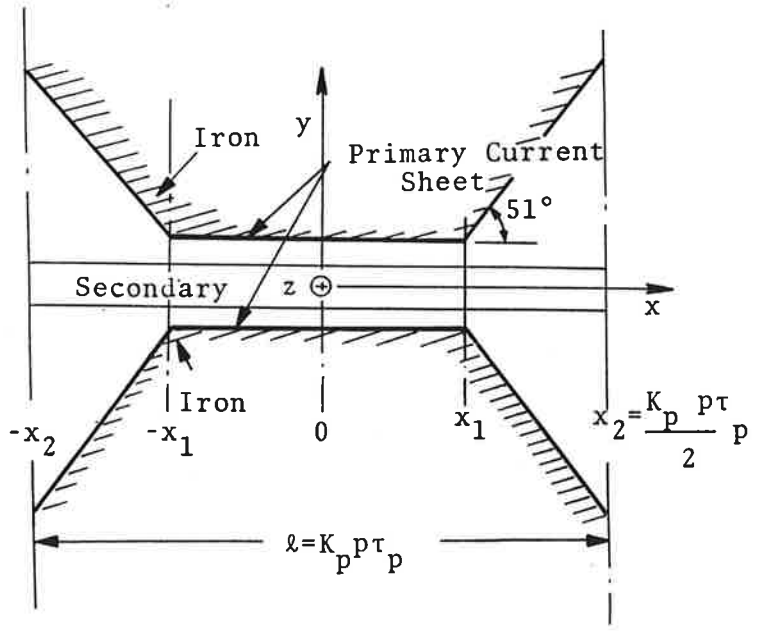

Figure 1b. Equivalent Mosebach LIM Mode (Side View)

permeance at both the ends and the sides of the motor. Thus it should provide a better description of magnetic boundary effects than the one-dimensional model. However, this is partly offset by the increased computer time required in the two-dimensional computer analysis. The one-dimensional computer program is used exclusively in this report for computer studies based on the Mosebach LIM model.

End views of the one- and two-dimensional models are shown in Figures 2a and 2b. The primary and secondary edges are located at transverse positions z_1 and z_2 respectively. The secondary half-thickness is y_1 and the core-to-core separation is $2y_{20}$.

The following assumptions are applicable to both versions of the Mosebach model:

a. The permeability of the ferromagnetic primary is infinite. The permeability of the secondary is equal to free-space permeability.

b. Primary and secondary currents are confined to the x-z plane.

c. Air-gap and secondary thickness are small compared with the pole pitch. Y-directed flux components are assumed uniform in both the airgap and the secondary.

d. Primary current density (surface) varies with distance (x) and time (t) according to exp (jkx + ωt).

The following additional assumptions are applicable to the one-dimensional model:

e. Secondary currents inside the primary region ($-z_1<z<z_1$) flow in the z direction.

f. Secondary currents outside the primary region flow in the x-direction. Current density in the secondary overhang (sidebar) is a uniform function of z.

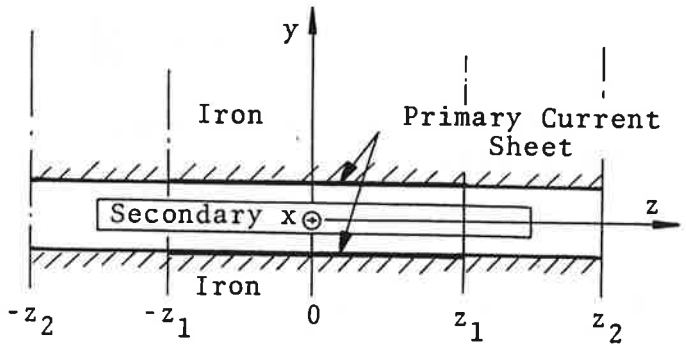

Figure 2a. End View of One-Dimensional Mosebach Model

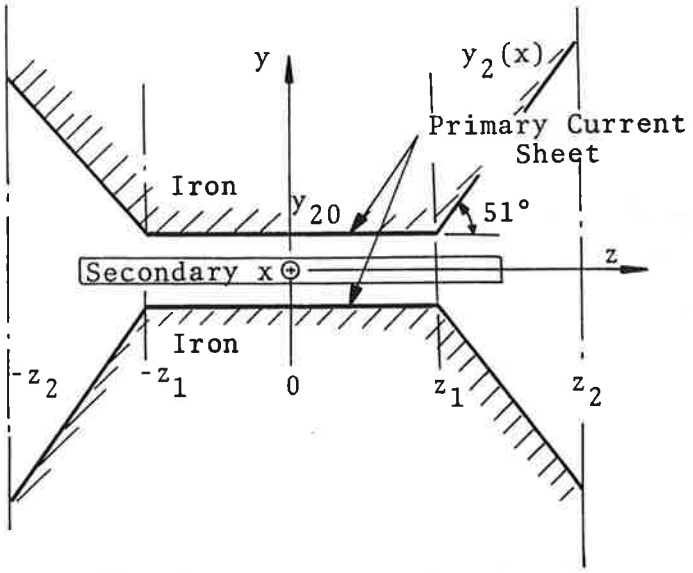

Figure 2b. End View of Two-Dimensional Mosebach Model

2.1.1 Magnetic Induction Equation: Two-Dimensional Model

The solution for the electromagnetic fields in the region between the two sides of the primary follows from Ampere's law with displacement current neglected and Faraday's law. Thus,

$$\overline{\nabla} \times \overline{H} = \overline{G}$$

$$\overline{\nabla} \times \overline{E} = - \frac{\alpha \overline{B}}{\alpha t} \tag{1}$$

where $\overline{G}$ is the secondary current density. For an isotropic medium moving with velocity $\overline{V}$, Ohm's law gives,

$$\overline{G} = \sigma \, (\overline{E} + \overline{V} \times \overline{B}) \tag{2}$$

Continuity of current inside the secondary requires,

$$\overline{\nabla} \cdot \overline{G} = 0 \tag{3}$$

Since assumption c requires the normal field to be independent of y, it is convenient to apply Ampere's law in integral form around the contour shown in Figure 3. Thus,

$$H(x+\Delta x) \cdot y_2(x+\Delta x) - H(x) \cdot y_2(x) = K_z \, \Delta x + G_z \cdot \Delta x \, y_1$$

or

$$\frac{\alpha}{\alpha x} \left(B_y y_2 \right) = \mu_o \left(K_z + G_z y_1 \right) \tag{4}$$

where $K_z^{\dagger}$ and G_z are the primary surface current density and secondary (volume) current density, respectively, in the z-direction.

---

†In the Mosebach notation, primary surface current density is given by A_z instead of K_z.

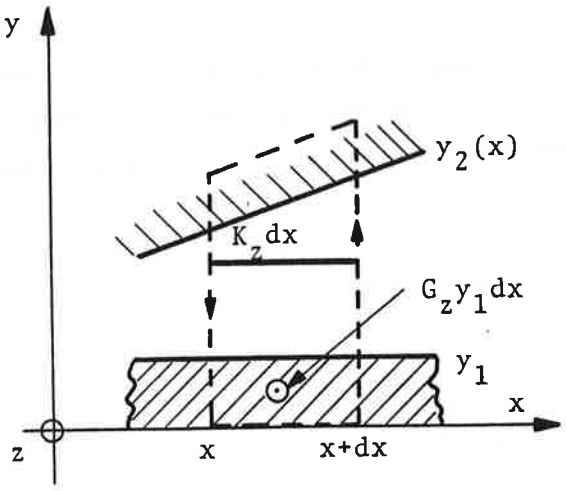

Figure 3. Contour Integration Used in Derivation of Magnetic Induction Equation

For the y field component, Faraday's law gives,

$$\frac{\alpha E_x}{\alpha z} - \frac{\alpha E_z}{\alpha x} = - \frac{\alpha B_y}{\alpha t} \tag{5}$$

where the electric field components E_x, E_z, given by Equation (2) take the form,

$$E_x = \frac{1}{\sigma} G_x$$

$$E_z = \frac{1}{\sigma} G_z - v B_y$$

Here v is the speed of the secondary in the x direction relative to the motor. Substituting E_x, E_z in Equation (5) gives,

$$\alpha G_z/\alpha x - \alpha G_x/\alpha z - \sigma\left[\alpha B_y/\alpha t + \alpha/\alpha x \left(v B_y\right)\right] = 0 \tag{6}$$

G_x can be eliminated using Equation (3) after taking the partial derivative of Equation (6) with respect to x.

$$\frac{\alpha^2 G_z}{\alpha x^2} + \frac{\alpha^2 G_z}{\alpha z^2} = \frac{\sigma\alpha}{\alpha x}\left(\frac{\alpha B_y}{\alpha t} + \frac{\alpha}{\alpha x}\left(v\ B_y\right)\right) = 0 \qquad (7)$$

If G_z is calculated from Equation (4), Equation (7) can be rewritten in the form expressing the field B_y, air-gap $y_2(x)$, and primary current density K_z in terms of the independent variables, x, z, and t.

$$\frac{\alpha^3}{\alpha x^3}\left(B_y y_2\right) + \frac{\alpha^3}{\alpha x \alpha z^2}\left(B_y y_2\right) - \mu_o \sigma y_1 \frac{\alpha}{\alpha x}\left[\frac{\alpha B_y}{\alpha t} + \frac{\alpha B_y}{\alpha x}\right] = \mu_o\left[\frac{\alpha^2 K_z}{\alpha x^2} + \frac{\alpha^2 K_z}{\alpha z^2}\right] \qquad (8)$$

A derivation of the corresponding equation for the one-dimensional model is given below.

2.1.2 Magnetic Induction Equation: One-Dimensional Model

The one-dimensional model assumes secondary currents flow in rectangular shaped paths as illustrated in Figure 4a. Inside the primary region, secondary currents flow in the z-direction; outside the primary region, secondary currents flow in the x-direction. No flux generated by the edge currents couples to the primary currents. The field inside the primary is constant in amplitude and phase over the width of the primary.

Faraday's Law of Induction, Equation (1) written in integral form, together with Ohm's law for the moving secondary, requires that for a contour C in the secondary enclosing a surface S,

$$\frac{1}{\sigma}\int_C \bar{G}\cdot d\bar{\ell} + \frac{\alpha}{\alpha t}\int_S \bar{B}\cdot\bar{n}\ da - \int_C \bar{V}\ x\ \bar{B}\cdot d\bar{\ell} = 0 \qquad (9a)$$

This general law is now applied to a current path having incremental length Δx in the x direction, but finite width spanning half of the secondary (Figure 4b).

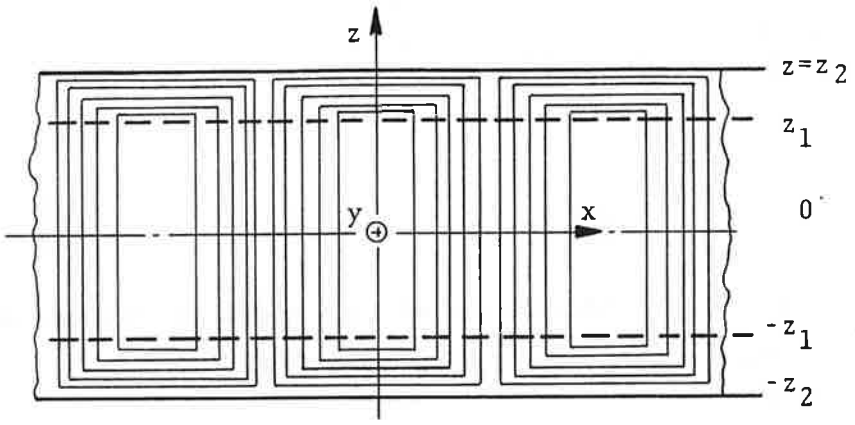

Figure 4a. Secondary Current Flow Pattern For One-Dimensional Model

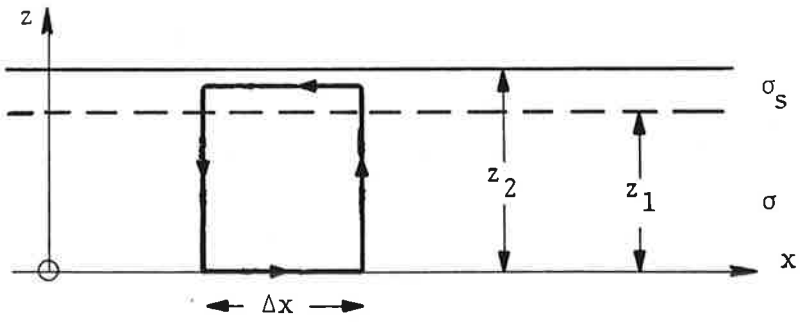

Figure 4b. Incremental Current Path For One-Dimensional Model

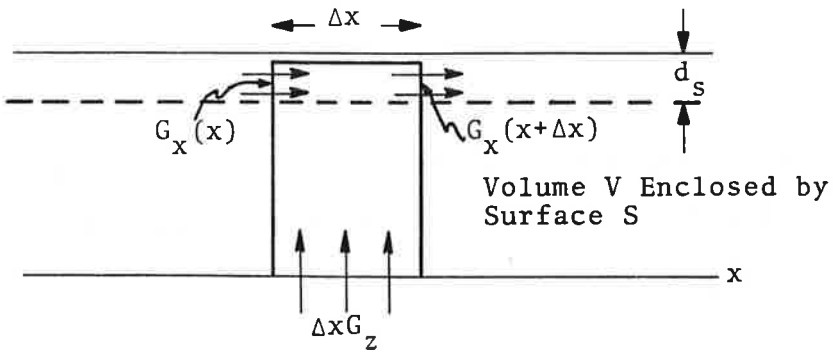

Figure 4c. Incremental Model For Current Continuity

$$\frac{1}{\sigma}\int_0^{z_1} G_z(x+\Delta x)dz - \frac{1}{\sigma}\int_0^{z_1} G_z(x)dz - \frac{G_x}{\sigma_s}\Delta x$$

$$- v\int_0^{z_1}\left[B_y(x+\Delta x) - B_y(x)\right]dz - \frac{\alpha}{\alpha t}\int_0^{z_1} B_y\,\Delta x\,dz = 0 \qquad (9b)$$

Here, the conductivity of the edges of the secondary is designated as σ_s as distinguished from σ describing the central region of the secondary.

Consistent with the one-dimensional model is the assumption that G_z and B_y in the region $-z_1<z<z_1$ are independent of z so that in the limit $\Delta x\to 0$, Faraday's law requires that

$$\frac{z_1}{\sigma}\frac{\alpha G_z}{\alpha x} - \frac{G_x}{\sigma_s} - z_1\left(\frac{B_y}{\alpha t} + \frac{\alpha B_y}{\alpha x}\right) = 0 \qquad (9c)$$

Just as an integral form of Faraday's law is used to bring the edge effects into the one-dimensional model, so also is an integral form of the current continuity equation, Equation (3), now brought in. With the help of the incremental section of secondary shown in Figure 4c, the continuity condition requires that

$$d_s\left[G_x(x+\Delta x) - G_x(x)\right] = G_z\,\Delta x \qquad (10a)$$

and in the limit it follows that

$$G_z = d_s\frac{\alpha G_x}{\alpha x} \qquad (10b)$$

where the thickness of the edge is defined as $d_s = z_2 - z_1$.

After taking the derivative with respect to x of Equation (9c), use can be made of Equation (10b) to eliminate G_x, and it follows that

$$\frac{z_1}{\sigma}\frac{\alpha^2 G_z}{\alpha x^2} - \frac{1}{\sigma_s} G_z - z_1\left[\frac{\alpha B_y}{\alpha t} + v\frac{\alpha B_y}{\alpha x}\right] = 0. \qquad (10c)$$

With the understanding that B_y and K_z are independent of z, Equation (4) can be introduced into this expression to eliminate G_z and give Mosebach's expression for the magnetic flux density as a function of the primary currents.

$$\frac{\alpha^3}{\alpha x^3}\left(B_y y_2\right) - \frac{\sigma}{z_1\sigma_s d_s}\frac{\alpha}{\alpha x}\left(B_y y_2\right) - \sigma y_1 \mu_o \frac{\alpha}{\alpha x}\left[\frac{\alpha B_y}{\alpha t} + v\frac{\alpha B_y}{\alpha x}\right] \qquad (11)$$

$$= \mu_o \frac{\alpha^2 K_z}{\alpha x^2} - \frac{\sigma\mu_o}{z_1\sigma_s d_s} K_z$$

The above equation determines the field distribution in the one-dimensional Mosebach model.

2.1.3 Solution of Magnetic Induction Equation: Two-Dimensional Model

The Mosebach treatment of the two-dimensional LIM model consists of expanding the spatial distributions of the airgap flux density $B_y(x,z)$, primary current density $K_z(x,z)$, and airgap function $y_2(x,z)$ along both the longitudinal (x) and transverse (z) axes of the LIM model. For this purpose, it is convenient to define a 'motor unit cell' having a length ℓ in the x direction and width $2\,z_2$ in the z direction. Inside the cell region, $B_y(x,z)$, $K_z(x,z)$, $y_2(x,z)$ are each described by a two-dimensional Fourier series, each term in the series being characterized by a wave propagation vector, $\bar{k}$, given by

$$\bar{k} = \bar{i}_x \frac{n\,2\pi}{\ell} + \bar{i}_z \frac{m\pi}{2\,z_2} \qquad (12a)$$

$$\bar{k} = \bar{i}_x\, n\, a + \bar{i}_z\, m\, b \qquad (12b)$$

where n, m are the harmonic orders associated with the x,z wave vector components. In practice, the unit cell length ℓ is set approximately equal to a multiple of the primary winding length. If KP denotes some integer greater than unity, then $\ell = KP \cdot P\tau_p$, where P is the number of (mmf) poles in the motor.† The width of the unit cell, $2\ z_2$, can be chosen equal to the secondary width. The two-dimensional function distributions then take the form,

$$B_y(x,z,t) = \mathrm{Re} \sum_n \sum_m B_{nm} e^{j(\omega t + nax + mbz)} \tag{13}$$

$$K_z(x,z,t) = \mathrm{Re} \sum_n \sum_m K_{nm} e^{j(\omega t + nax + mbz)} \tag{14}$$

$$y_2(x,z,t) = \sum_\lambda \sum_\mu Y_{\lambda\mu} e^{j(\lambda ax + \mu bz)} \tag{15}$$

The harmonic amplitudes K_{nm} and $Y_{\lambda\mu}$ are found by taking the Fourier transforms of the known spatial distributions of primary current and airgap spacing respectively.

The substitution of Equations (13), (14), (15) in (8) yields the following equation relating the amplitude cofficients B_{nm}, K_{nm}, and $Y_{\lambda\mu}$.

$$\sum_m \sum_n \sum_\mu \sum_\lambda \left[-j(n+\lambda)^3 a^3 - j(n+\lambda) a (m+\mu)^2 b^2 \right] Y_{\mu\lambda}\ B_{nm} e^{j\left(\omega t + (n+\lambda)ax + (m+\mu)bz\right)}$$

$$- \sigma y_1 \mu_o \sum_n \sum_m (jna)(j\omega + jvna) B_{nm}\ e^{j(\omega t + nax + mbz)} \tag{16}$$

$$= \mu_o \sum_n \sum_m \left[(jna)^2 + (jmb)^2 \right] K_{nm} e^{j(\omega t + nax + mbz)}$$

†Mosebach uses P_o to denote number of pole pairs.

Transforming the summation indices n, m, in Equation (16),

$$m + \mu \rightarrow m$$

$$n + \lambda \rightarrow n$$

and collecting coefficient of terms with identical space and time dependences,

$$\sum_{\mu}\sum_{\lambda} Y_{\mu\lambda} B_{m-\mu,n-\lambda} + j\, r \frac{s_n\, y_{20}}{\left(\frac{2n}{K_p P}\right)^2 + \left(\frac{m\tau_p}{2z_2}\right)^2} B_{nm} = - j\mu_o \frac{K_{nm}}{\left(\frac{2n}{K_p P}\right)\frac{\pi}{\tau_p}} \tag{17}$$

where r is the magnetic Reynolds number

$$r = \frac{\mu_o \omega \sigma y_1}{\left(\frac{\pi}{\tau_p}\right)^2 y_{20}} \tag{18a}$$

and s_n is the harmonic slip given by

$$s_n = 1 - \left(\frac{2\, n}{K_p P}\right)(1 - s) \tag{18b}$$

The quantity y_{20} in Equation (17) denotes the half-spacing between primary cores (see Figure 2b). Equation (17) describes a set of linear, complex equations relating the unknown flux density amplitudes, B_{nm}. In matrix notation, the equation takes the form,

$$\left([Y] + j\, [R]\right) \cdot \bar{B} = \bar{K} \tag{19}$$

[Y] is a real, quadratic matrix and is independent of slip. [R] is a real, diagonal matrix with slip-dependent elements. The solution of Equation (19) is obtained by setting,

$$\bar{B} = \bar{B}_r + j\,\bar{B}_i$$

$$\bar{K} = \bar{K}_r + j\,\bar{K}_i$$

and solving for the real and imaginery parts of B.

$$\bar{B}_r = \frac{\bar{K}_r - \left[R\right]\cdot\left[Y^{-1}\right]\cdot\bar{K}_i}{[Y] + [R][Y^{-1}][R]}$$

$$\bar{B}_i = \frac{\bar{K}_i + \bar{B}_r\cdot[R]}{[Y]}$$

2.1.4 Solutions of Magnetic Induction Equation: One-Dimensional Model

The procedure for solving the one-dimensional field equation is identical in principle to that used in the solution of the two-dimensional equation. In the one-dimensional model, the airgap field B_y, primary current density K_z, and airgap spacing function y_2 are expanded in Fourier series along the x axis.

$$B_y(x,t) = \mathrm{Re}\left\{\sum_{n=-\infty}^{\infty} B_n e^{j(\omega t + nax)}\right\} \tag{20}$$

$$K_z(x,t) = \mathrm{Re}\left\{\sum_{n=-\infty}^{\infty} K_n e^{j(\omega t + nax)}\right\} \tag{21}$$

$$y_2(x) = \sum_{\lambda=-\infty}^{\infty} Y_\lambda e^{j(\lambda ax)} \tag{22}$$

Substituting the above equations in Equation (11) gives,

$$\sum_n \sum_\lambda - j\left[(n+\lambda)^3 a^3 + \frac{\sigma}{\sigma_s z_1 d_s}(n+\lambda)a\right] Y_\lambda B_n e^{j\left[\omega t + (n+\lambda)ax\right]}$$

$$+ \sum_n \mu_o \sigma \omega y_1 na \left(1 + \frac{vna}{\omega}\right) B_n e^{j\left[\omega t + nax\right]}$$

$$= - \mu_o \sum_n \left[(na)^2 + \frac{\sigma}{\sigma_s z_1 d_s}\right] K_n e^{j\left[\omega t + nax\right]} \qquad (23)$$

Transforming the summation indice n in the first summation, $n+\lambda \rightarrow n$, and collecting coefficients with common space and time dependence,

$$\sum_\lambda Y_\lambda \; B_{n-\lambda} \quad + j \; \frac{r'_n \; s_n y_i \; B_n}{n^2} \quad = - j \; \frac{\mu_o}{na} \; K_n \qquad (24)$$

where r'_n is the magnetic Reynolds number associated with the fundamental spatial harmonic in the 'motor unit cell', i.e.,

$$r'_n = \frac{\mu_o \sigma \omega}{a^2 \left(1 + \frac{\sigma}{\sigma_s z_1 d_s a^2 n^2}\right)} \qquad (25)$$

and s_n is as defined by Equation (18b). In matrix form, the above equation becomes,

$$[Y] + j[R] \cdot \bar{B} = \bar{K} \qquad (26)$$

For a system comprising the set of harmonics $-2 \leq n \leq 2$, [R] and [Y] take on the form,

$$[R] = \begin{bmatrix} \frac{r'_{-2} s_{-2}}{4} & 0 & 0 & 0 & 0 \\ 0 & \frac{r'_{-1} s_{-1}}{1} & 0 & 0 & 0 \\ 0 & 0 & 0 & 0 & 0 \\ 0 & 0 & 0 & \frac{r'_1 s_1}{1} & 0 \\ 0 & 0 & 0 & 0 & \frac{r'_2 s_2}{4} \end{bmatrix} \qquad [Y] = \begin{bmatrix} Y_0 & Y_{-1} & Y_{-2} & Y_{-3} & Y_{-4} \\ Y_1 & Y_0 & Y_{-1} & Y_{-2} & Y_{-3} \\ Y_2 & Y_1 & Y_0 & Y_{-1} & Y_{-2} \\ Y_3 & Y_2 & Y_1 & Y_0 & Y_{-1} \\ Y_4 & Y_3 & Y_2 & Y_1 & Y_0 \end{bmatrix}$$

where r' is given by Equation (25) and the matrix elements Y_λ are determined from

$$Y_\lambda = \int_{-\ell/2}^{\ell/2} y_2(x) e^{-j\lambda ax} dx$$

$\bar{B}$ and $\bar{K}$ are complex vectors

$$\bar{B} = \begin{bmatrix} B_{-2} \\ B_{-1} \\ 0 \\ B_1 \\ B_2 \end{bmatrix} \qquad \bar{K} = \begin{bmatrix} K_{-2} \\ K_{-1} \\ 0 \\ K_1 \\ K_2 \end{bmatrix}$$

The solution for the real and imaginery parts of B are given by

$$B_r = \frac{\bar{K}_r - [R] \cdot [Y^{-1}] \cdot \bar{K}_i}{[Y] + [R] \cdot [Y^{-1}] \cdot [R]} \tag{27}$$

$$B_i = \frac{\bar{K}_i + \bar{B}_r \cdot [R]}{[Y]} \tag{28}$$

The current density harmonic K_n is found by taking the Fourier transform of the primary current distribution over the length ℓ of the unit cell. In practice, it is desirable to compute the current density harmonics for each phase winding since the "phase harmonics" are required for the subsequent constant voltage analysis. Thus if K_n^k denotes the nth harmonic of the kth phase,

$$\bar{K}_n^k = \frac{1}{\ell} \int_{-\ell/2}^{\ell/2} f_k(x) \; \bar{K}_z^k(x) e^{-jnax} dx \tag{29}$$

where $f_k(x)$ is a 'slot distribution function' which defines the occupancy of a given stator slop, i.e.,

$f_k(x) = 0$ slot unoccupied by kth phase winding

$f_k(x) = 1$ slot occupied by kth phase winding; reference phase equals zero

$f_k(x) = -1$ slot occupied by kth phase winding; reference phase equals 180 degrees

In closed form, $\bar{K}_n^k$ can be expressed as,

$$\bar{K}_n^k = \left(a_{nk} - jb_{nk}\right) \cdot \bar{K}^k \tag{30}$$

where K^k is the primary current density amplitude

$$\bar{K}^k = \frac{3Nq}{\tau_p} \bar{I}^k \tag{31}$$

In a similar manner it is possible to express the nth harmonic of flux density associated with the kth primary phase as,

$$\bar{B}_n^k = - \frac{j\mu_o}{an\ y_{20}} \left(c_n^k - jd_n^k\right) \bar{K}^k \tag{32}$$

where the complex coefficient $c_n^k - jd_n^k$ determines the amplitude and phase of B_n^k.

2.1.5 Constant Voltage Source

The solution for the case of a LIM with constant voltage excitation requires the calculation of currents flowing in each phase winding produced by the fixed input voltage excitation. Each phase current is uniquely determined once the input impedance of the given phase winding is known.

The equation for the voltage drop in the kth phase winding of the LIM is,

$$V^k = \left(R_1^k + jX_1^k\right) \cdot I^k + V_{induced}^k \tag{33}$$

The first term on the right-hand side includes the winding resistance and primary leakage reactance. The second term describes the voltage induced by the air-gap field as a result of currents flowing in the different phase windings of the motor. The induced voltage can be computed by integrating the electric field over the length of the conductors in the given phase. For the nth harmonic flux wave,

$$E_n = \frac{\omega B_n}{n\,a} \tag{34}$$

Expressing B_n in terms of phase currents I_k using Equations (31) and (32),

$$E_n = -\,j\frac{\omega}{na}\,\frac{\mu_o}{na\,y_{20}}\,\frac{3Nq}{\tau_p}\sum_k I^k\left(c_n^k - jd_n^k\right) \tag{35}$$

The phase voltage found by integrating the electric field $E_z(x,t)$,

$$E_z(x,t) = \sum_n E_n e^{j(\omega t + nax)} \tag{36}$$

over all conductors of the k'th phase is,

$$V^{k'} = 2z_1 \int_{-\ell s/2}^{\ell s/2} E_z(x,t)\,\frac{3Nq}{\tau_p}\,f^{k'}(x)\,dx$$

$$= -\,j\frac{\omega\mu_o 2z_1}{a^2\,y_{20}}\left(\frac{3Nq}{\tau_p}\right)^2 \ell \sum_k I^k \sum_n \left(c_n^k - jd_n^k\right)\cdot\left(a_n^{k'} + jb_n^{k'}\right) \tag{37}$$

The voltages in a three-phase system can be written in the form,

$$\begin{pmatrix} V^1 \\ V^2 \\ V^3 \end{pmatrix} = \left[\begin{array}{c|c|c} Z_{11} + R_1^1 + jX_1^1 & Z_{12} & Z_{13} \\ \hline Z_{21} & Z_{22} + R_1^2 + jX_1^2 & Z_{23} \\ \hline Z_{31} & Z_{32} & Z_{33} + R_1^3 + jX_1^3 \end{array}\right] \begin{pmatrix} I_1^1 \\ I_1^2 \\ I_1^3 \end{pmatrix} \quad (38)$$

Identifying the impedance elements of the above matrix with Equation (37) gives for the mutual impedance between the k and k'th phases.

$$Z_{kk'} = - j \frac{\omega \mu_o 2 z_{1\ell}}{a^2 y_{20}} \left(\frac{3Nq}{\tau_p}\right)^2 \sum_{n=-\infty}^{\infty} \frac{\left(c_n^k - jd_n^k\right)\cdot\left(a_n^{k'} + jb_n^{k'}\right)}{n^2} \quad (39)$$

2.1.6 LIM Output Parameters

The electromagnetic characteristics of a LIM can be determined once the air-gap flux density and secondary current density have been found for the specified primary current density excitation. The nth harmonic of the second current density G(n) is related to the nth harmonic of air-gap flux density B(n),†

$$G(n) = \frac{\sigma \omega s_n}{a\ n} B(n) \quad (40)$$

The thrust F_x is found by integrating the force density over the volume of the secondary.

$$F_x = - \int_V 1/2\ \mathrm{Re}\left(G_z\ B_y^*\right) dV \quad (41)$$

†For clarity, the harmonic order is indicated in the parenthesis rather than subscripts as previously given.

Substituting the Fourier series expansions for G_z, B_y in the above equation and integrating,

$$F_x = \sum_n F_x(n) = 2z_1 y_1 K_p P\tau \sum_n \left(B(n)G^*(n) + B^*(n)G(n) \right) \qquad (42)$$

Mechanical power P_m, is equal to the product of thrust and motor speed. It can also be expressed as the summation of the products of thrust harmonics and speed harmonics. Since the nth harmonic wave has a speed $v(n)=(1-s_n)\omega/na$, the mechanical power is

$$P_m = \sum_n P_m(n) = \sum_n F_x(n) \ (1-s_n) \ \frac{\omega}{a\ n} \qquad (43)$$

The air-gap power which is the real power tranferred to the secondary, is given by

$$P_{ag} = \sum_n P_{ag}(n) - \sum_n F_x(n) \ \frac{\omega}{a\ n} \qquad (44)$$

The secondary power loss equal to the heating losses in the secondary is

$$P_{sec} = \sum_n P_{sec}(n) = \sum_n F_x(n) \ \frac{s_n}{a\ n} \qquad (45)$$

The form which these harmonic spectra takes is illustrated in Figure 6 for the TLRV operating at a speed of 300 MPH.

2.2 MOSEBACH ONE-DIMENSIONAL COMPUTER PROGRAM

2.2.1 Choice of Fourier Cell Length ℓ and Maximum Harmonic Order NMAX

The Mosebach theory uses Fourier series expansions to describe the spatial distributions of airgap flux density and airgap function $y_2(x)$. These series are expanded on the basis of a periodic

length in the x direction equal approximately to some multiple of the motor (primary) length. Thus $\ell = KP\ P\ \tau_p$ where KP is some integer greater than unity. The criteria for choosing ℓ is determined by the requirement that the flux density at the exit end of the motor cell be sufficiently attenuated so as to have negligible effect on the boundary conditions at the entrance end of the motor cell. A choice of cell (periodicity) length which results in the flux being attenuated to one percent of its maximum value is considered adequate. If ℓ is chosen larger than necessary to satisfy the above condition, the number of harmonics required to describe the Fourier distribution becomes unduly large leading to excessively high computing times.

The dependence of LIM motor characteristics on the choice of KP is illustrated in the table below in which LIM thrust, airgap power, and secondary power loss are computed for the TLRV LIM for KP = 2, 4, and 8. Motor conditions correspond to primary phase current of 530 amperes, excitation frequency of 165 Hertz, and speed equal to 300 mph. In order to include the same relative range of harmonics in the spectral distribution, the maximum harmonic order NMAX, was increased roughly proportional to KP. Sketches showing the airgap functions for the different values of KP are given in Figure 5.

The results given in Table 1 show that airgap power and secondary power loss are relatively insensitive to KP (cell length) while the thrust shows a functional dependence when KP varies from 2 to 4. For KP greater than 4, the motor output parameters vary only slightly, with no change being observed in LIM thrust. For all examples considered in Table 1, the cell length is sufficient to insure attenuation of the airgap flux density to one percent of maximum value.

NMAX specifies the range of harmonic orders, $-NMAX \leq n \leq NMAX$, required to describe the field and current distributions in the motor. Experience has shown that a value of NMAX equal to three times the harmonic order of peak flux density amplitude is generally adequate. Table 2 gives the TLRV LIM output parameters computed

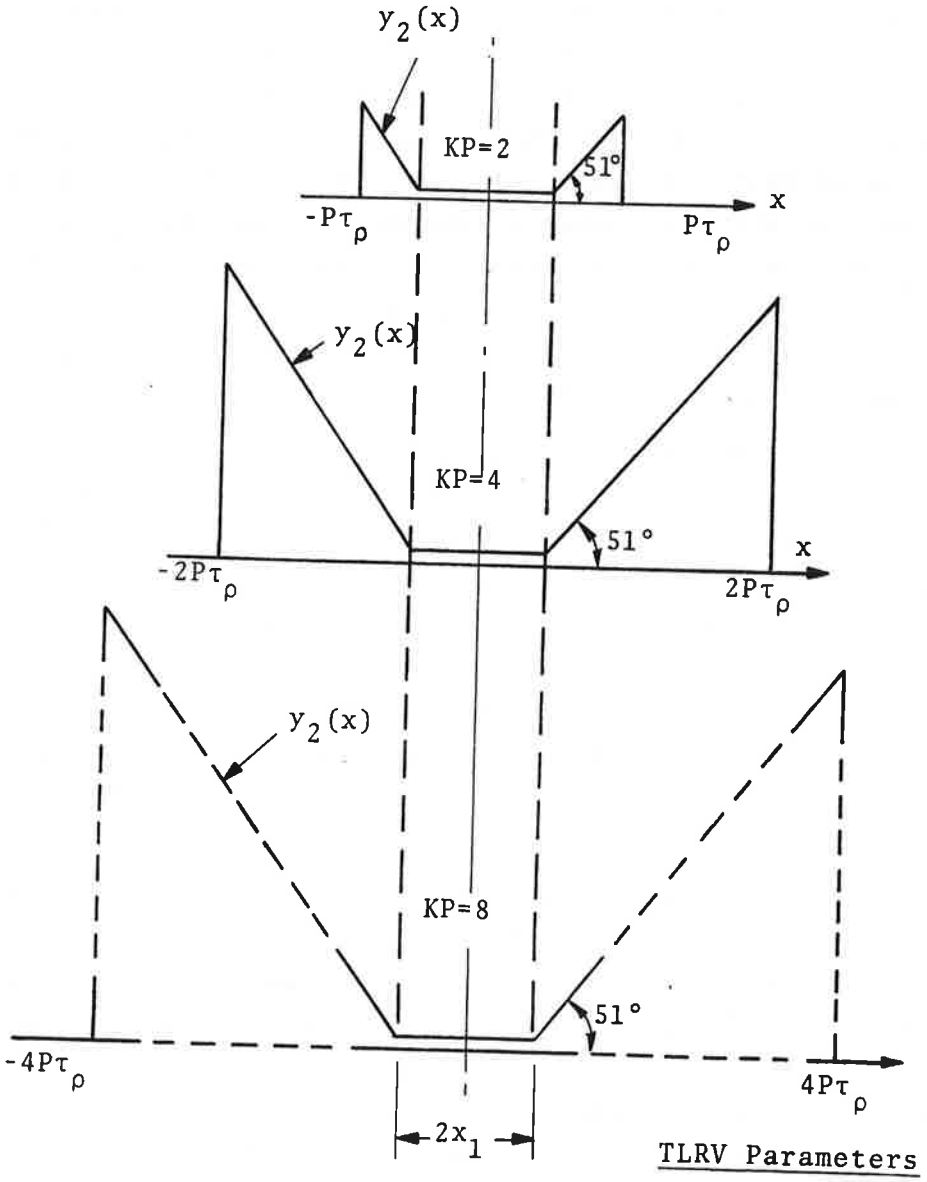

Figure 5. TLRV Airgap Functions for Different Values of KP

TABLE 1. TLRV OUTPUT PARAMETERS VERSUS NORMALIZED FOURIER CELL LENGTH

KP	NMAX	THRUST (N/side)	AIRGAP POWER (KW/side)	SECONDARY POWER LOSS (KW/side)
2	15	1569	668.66	458.16
4	25	1663	673.97	450.94
8	50	1663	670.30	449.21

TABLE 2. TLRV OUTPUT PARAMETERS VERSUS MAXIMUM HARMONIC ORDER

NMAX	THRUST (N/side)	AIRGAP POWER (KW/side)	SECONDARY POWER LOSS (KW/side)
8	4593	801.8	185.7
10	4550	800.6	190.3
16	4497	796.9	193.7
24	4481	797.1	196.1
50	4450	797.2	200.3

for five NMAX values for the LIM operated at 530 amperes/phase, an excitation frequency of 200 Hertz, and speed of 300 mph. With KP equal to two, the peak field and current harmonics corresponded to the fifth harmonic order. Table 2 shows that an increase in NMAX from 16 to 50 results in only a one percent change in thrust and an almost insignificant change in airgap power. The dependence of secondary power loss on NMAX is somewhat greater, due to the fact that a large number of harmonics is necessary to describe the sharp peak in secondary current which normally exists at the trailing edge of the LIM at high speeds.

The computed spectral distributions of flux density, thrust, airgap power, and secondary power are shown in Figure 6 for the motor conditions applicable to Table 2. The form of the spectral distribution suggests that little loss in accuracy results from

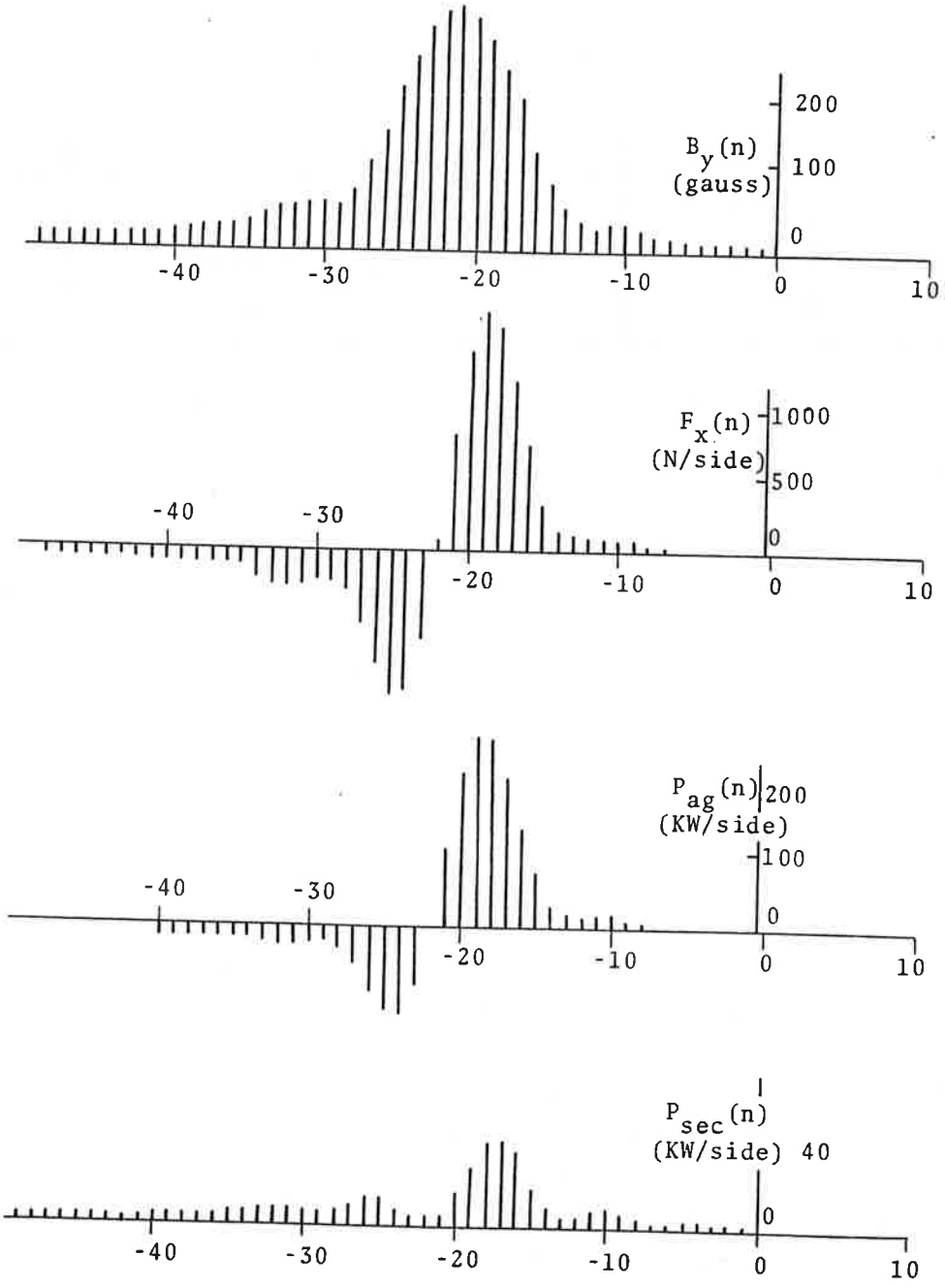

Figure 6. Harmonic Amplitudes for TLRV LIM Air-Gap Flux Density, Thrust, Air-Gap Power, and Secondary Power Loss. KP=8; Motor Speed = 300 MPH; Excitation Efficiency = 165 Hz

restricting the harmonic orders to negative values. In its present form, the Mosebach computer program sums over equal numbers of positive and negative harmonic orders so that some modification of the program to limit the region of harmonic summation would seem worthwhile.

2.3 BOUNDARY-EFFECT CONSIDERATIONS

2.3.1 Magnetic End-Effect

The effect of the finite length of primary iron (core) on LIM performance or so-called magnetic end-effect, can be important at high motor speeds and low slip-frequencies. The magnetic end-effect is examined in this section using the example of the TLRV operating at rated speed and stator current excitation. Two LIM models are considered: the first has a finite length primary iron (Model A) and the second has continuous primary iron (Model B). The difference in LIM characteristics of the two models describes the effect of the limited iron length on motor performance.

The TLRV output characteristics are computed at rated speed (300 mph) and stator current (530 amperes/phase) as a function of excitation frequency. Motor parameters required for the calculations are summarized in Table 4. To insure convergence of the Fourier series for the case of the continuous primary iron (Model B), it is necessary to increase the length of the periodic cell to about eight times the length of the primary winding. The computer parameters used in the calculations are given below:

MODEL	KP	NMAX
A	2	15
B	8	50

Figure 7 presents the LIM thrust for Models A and B as a function of stator excitation frequency. The magnetic end-effect as represented by the difference in the curves becomes quite small above 200 Hz but has a large effect at lower frequencies. Thus at a frequency of 165 Hz corresponding to a slip of 0.0928, LIM thrust is reduced approximately fifty percent by magnetic end-effect.

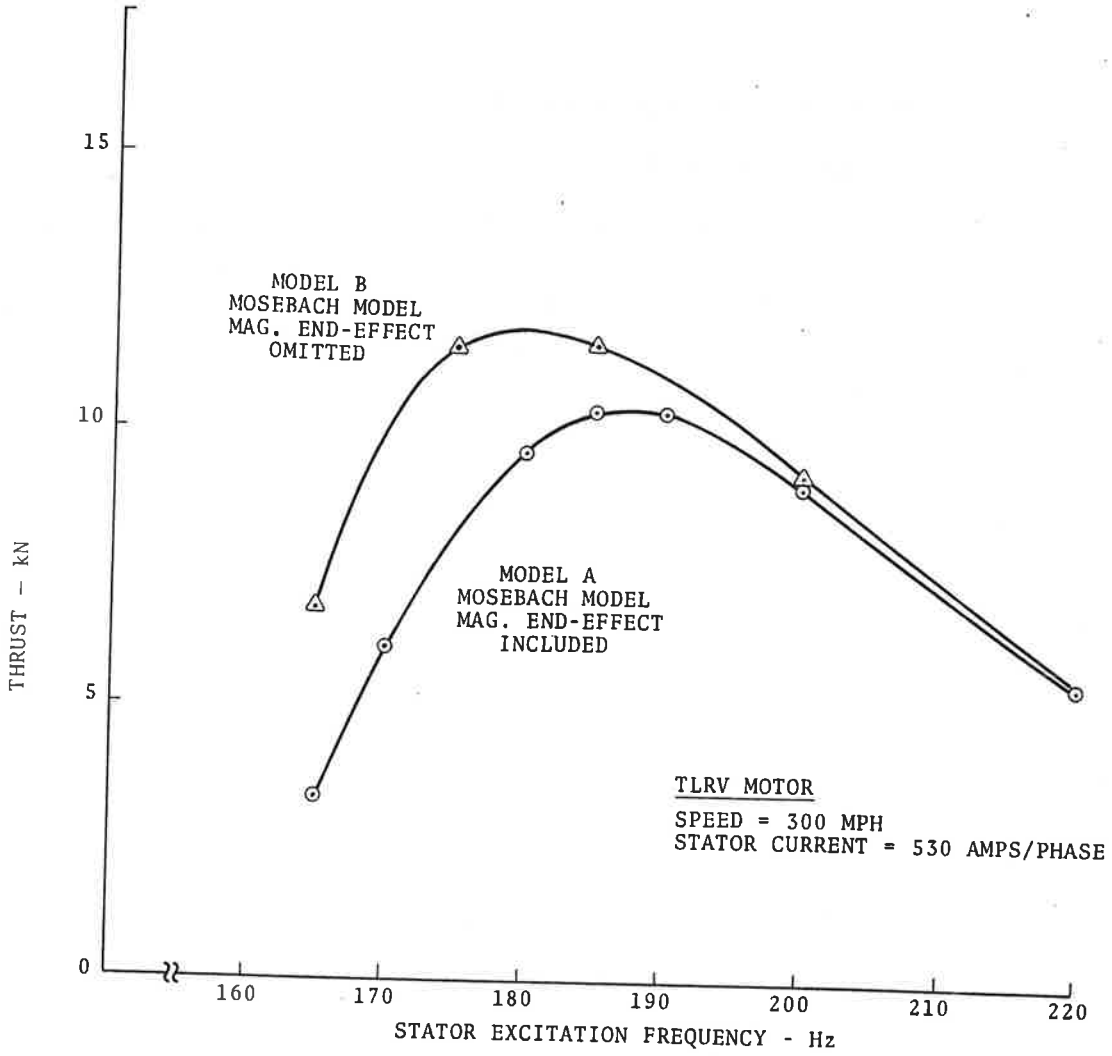

Figure 7. TLRV Thrust Predicted by Mosebach Theory When Magnetic End-Effects are Included for LIM Model and Neglected in LIM Model

Figure 8 presents the airgap power P_{ag}, mechanical power P_m, and secondary power P_{sec} predicted by the Mosebach theory for finite length and continuous primary iron models. Airgap power is almost unaffected by the length of the primary iron core, in contrast to the mechanical and secondary powers which are considerably affected by the length of the primary iron. This suggests that magnetic end-effects do not affect the total real power to the motor but alter the division of this power into usable mechanical work and secondary power loss (heating).

The power factor was also computed for the same set of conditions applicable to Figures 7 and 8. The change in power factor with magnetic end-effect included was relatively small, and typically increased four percent at a slip of .0928. The results suggest that LIM real and reactive power components are insensitive to the extention of iron beyond the region of the primary winding.

The airgap flux density along the longitudinal (x) axis of the motor is insensitive to magnetic end-effect within the primary ($-x_1 \leq x \leq x_1$) but can be strongly dependent on magnetic end-effect in the region outside the primary ($x \geq |x_1|$). Figure 9 shows the flux density amplitude computed for the TLRV at 300 mph (530 amperes/phase, 165 Hz) for continuous primary ferromagnetic region and a finite ferromagnetic region given by the actual core size. The trailing flux density in the exit end of the LIM attenuates exponentially with distance in both cases. This is illustrated in Figure 10 in which the log of the flux density amplitude is plotted against distance along the x axis. The linear slopes of these flux attenuation characteristics yield the attenuation constants given below. Also shown is the corresponding attenuation constant predicted by the Yamamura theory[3] for the case of continuous primary iron.

	Mosebach Model	Yamamura Model
Continuous iron primary	$0.211m^{-1}$	$0.25m^{-1}$
Finite iron primary	$1.61m^{-1}$	-

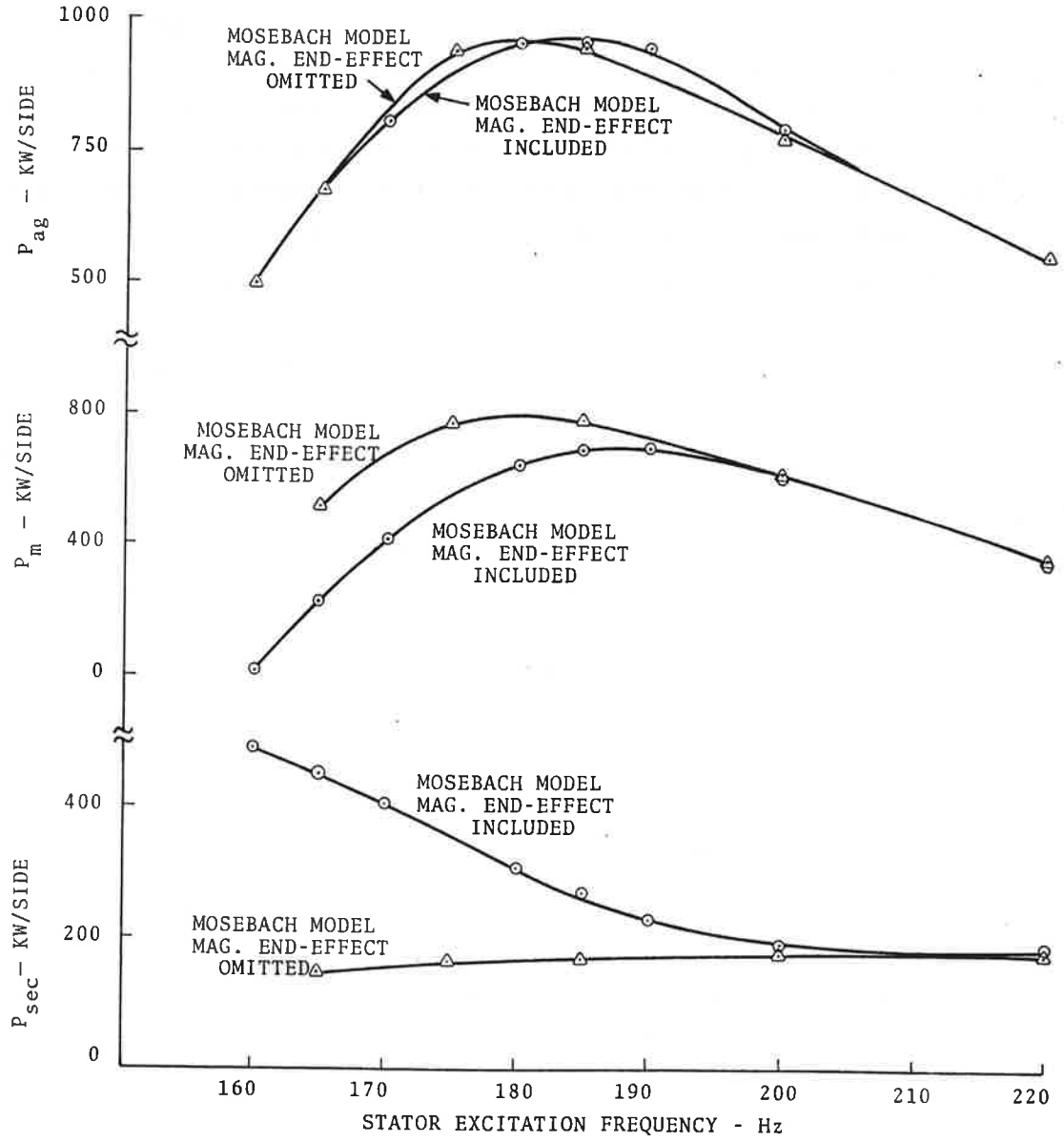

Figure 8. TLRV Air-Gap Power, Mechanical Power, and Secondary Power Predicted by Mosebach Theory When Magnetic End-Effects are Included in LIM Model and Neglected in LIM Model

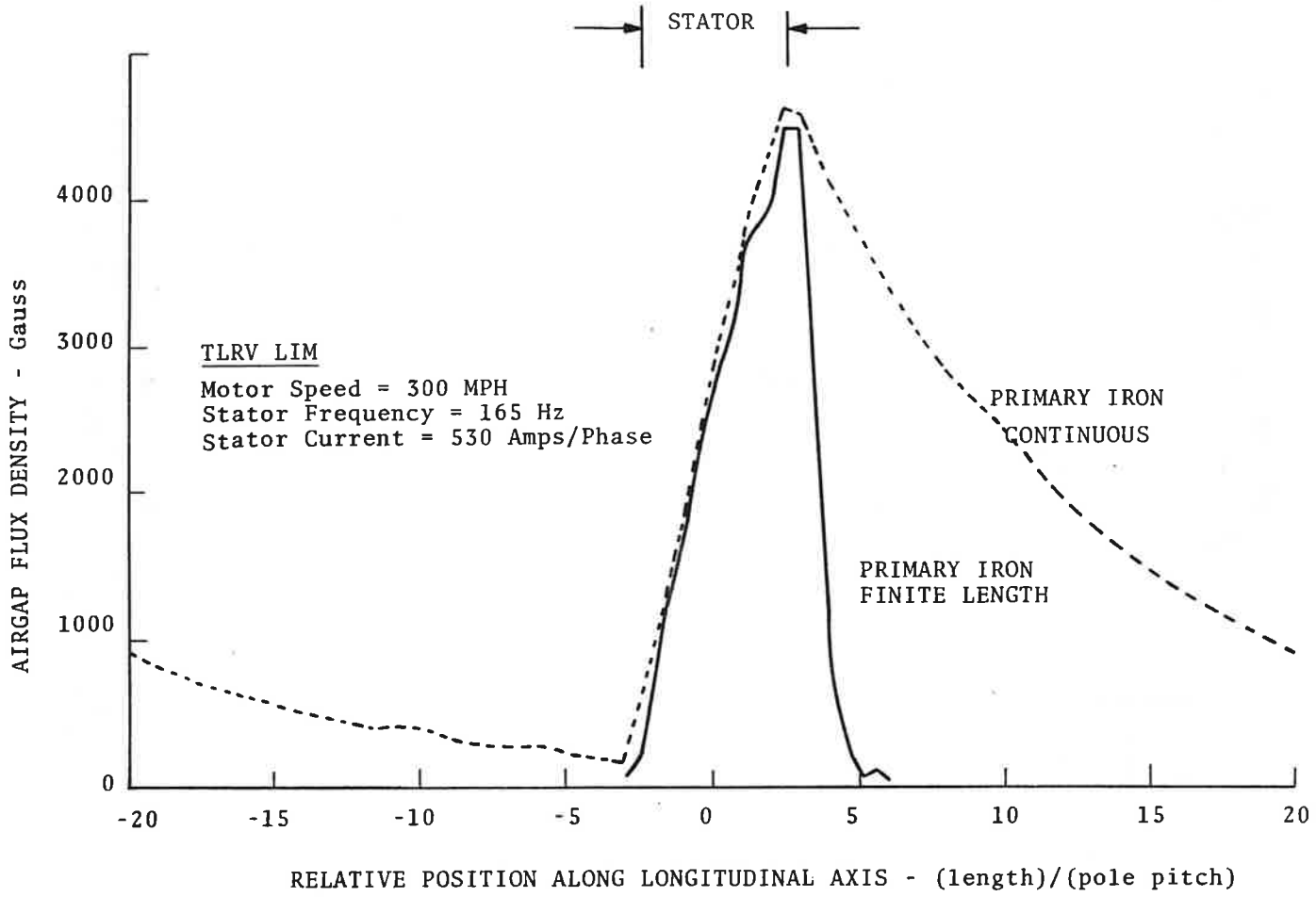

Figure 9. Air-Gap Flux Density for TLRV LIM as Predicted by Mosebach Theory When Magnetic End-Effects are Included in LIM Model and Neglected in LIM Model

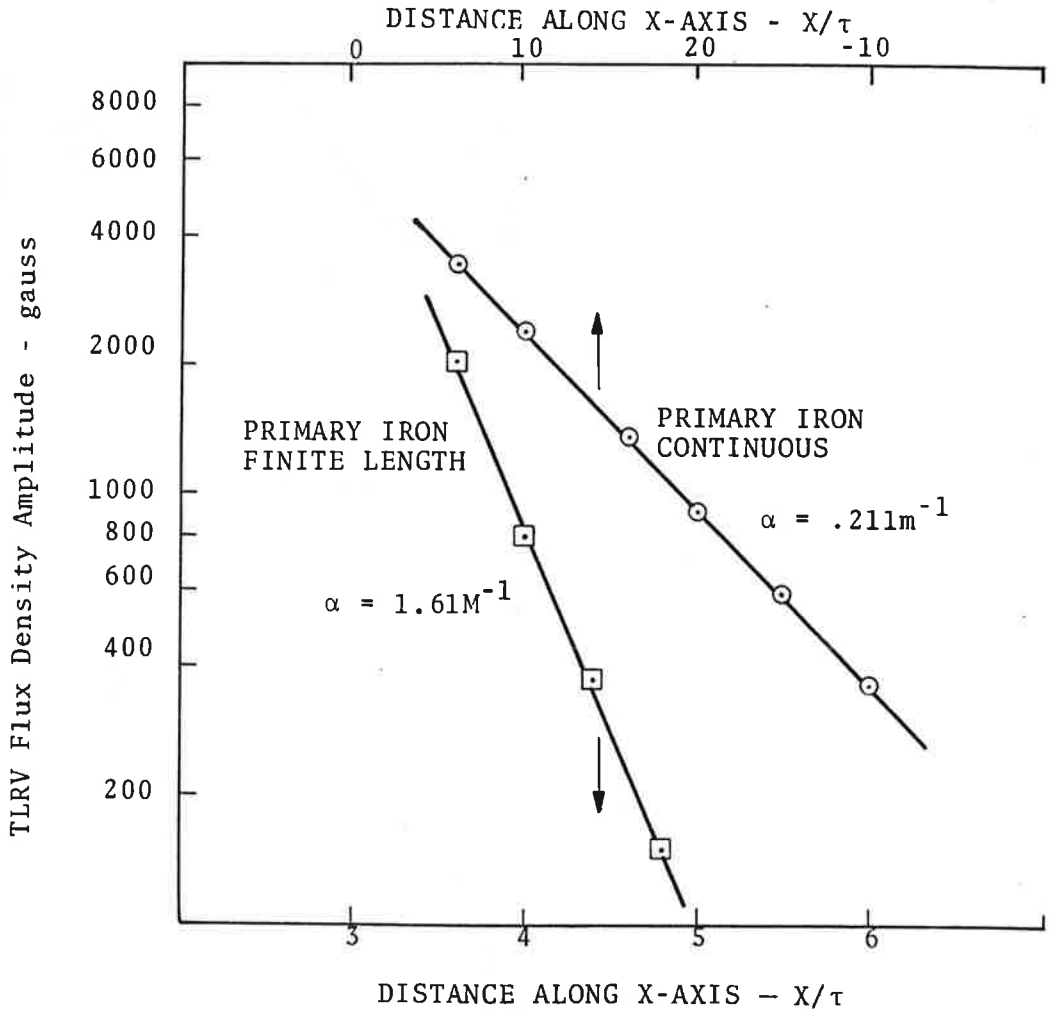

Figure 10. Semilog Plot of Air-Gap Flux Density of TLRV LIM as Predicted by Mosebach Theory when Magnetic End-Effects are Included in LIM Model and Neglected in LIM Model

2.3.2 Transverse Edge-Effect: Mosebach Versus Bolton Treatments

The Mosebach treatment of the transverse edge-effect differs considerably from the approach used by Bolton.[5] In the Mosebach one-dimensional model, the actual secondary overhang is replaced by ficticious sidebars which serve to conduct all the longitudinally directed currents flowing in the secondary. The secondary current is also assumed to flow in rectangularly-shaped patterns (Figure 4a). These flow patterns remain independent of frequency so that the mutual coupling (inductance) between primary and secondary is independent of frequency. Changes in the secondary impedance (as seen by the primary) are then identified with changes in the secondary leakage inductance and secondary resistance, rather than with changes in the secondary magnetizing inductance and secondary resistance. In the Bolton model, the finite secondary width does not cause any restriction in the secondary current paths. Secondary currents flow in patterns described by Bolton as 'television screen' or 'distorted television screen' shaped patterns. These flow patterns change with slip frequency in order to accommodate flow paths of minimum secondary reactive impedance. In terms of equivalent circuit parameters, this requires a slip-dependent mutual inductance and secondary resistance.

The secondary current flow pattern was computed by Mosebach using a two-dimensional theory which allows for unrestricted current flow in the x, z plane. His results are shown in Figure 11 for two values of effective Reynolds number (r's). For large r's the flow pattern is nearly rectilinear and similar to the flow lines shown sketched in Figure 4a. For r's equal to five, a more nearly television-screen type pattern results. Since the one-dimensional Mosebach theory is restricted to rectilinear-type flow patterns, it should yield more accurate results when applied under conditions of large effective Reynolds numbers.

The Mosebach treatment of the transverse edge-effects leads to an effective secondary conductivity σ^*, which depends on the longitudinal harmonic order n,

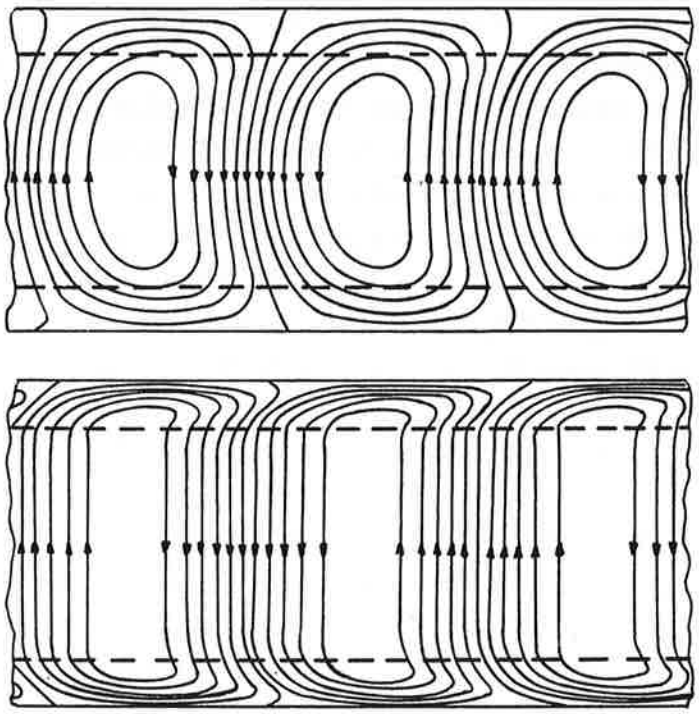

Figure 11. Current Flow in Secondary for Different r's Values

$$\sigma^* = \frac{\sigma}{1 + z_1 d_s a^2 n^2} \tag{46}$$

The effect of the sidebars is contained in the term in the denominator which is a function of the overhang distance d_s, the half-core width z_1, and wave vector amplitude a n. Since the overhang distance d_s cannot be zero in the Mosebach model, as otherwise there remains no return path for the secondary currents, this poses a problem in treating LIMs with zero or near-zero overhand distances.

The Bolton treatment of the transverse edge-effect leads to an effective secondary resistance in parallel with an effective magnetizing reactance given by

$$R_2' = K_2 \cdot R_2$$

$$X_m' = K_1 \cdot X_m$$

where K_1 and K_2 are defined by,

$$K_1 = K_x \frac{1 + s^2 G^2 K_R^2 / K_X^2}{1 + s^2 G^2} \qquad K_2 = \frac{K_X}{K_R} K_1$$

For the TLRV operating at 165 Hz, K_1 varies from 1.0 to 0.4 as the slip goes from 0.0 to 1.0, and K_2 varies from 2.47 to 2.72 as the slip goes from 0.0 to 1.0. The latter range of parameter values is to be compared with the denominator of Equation (46) which equals 2.32 evaluated at the harmonic order of peak flux density amplitude. (For KP equal to two, the peak flux density harmonic occurs at n equal to five.)

In the Yamamura theory of linear induction motors,[6] the Bolton factors K_1, K_2 are used to correct for the finite width of the LIM, but in a different manner than used by Bolton in his analysis. The Yamamura treatment assumes X_m remains constant and secondary conductivity is modified by the factor K_1/K_2. In addition the primary current density is replaced by K_1 x (primary current density. When applied correctly, the Yamamura treatment is equivalent to that of Bolton.

It is interesting to compare the different results which would have been obtained had the Bolton factors been used in place of Equation (46) to compensate for edge-effect. Table 3 gives the thrust and airgap power for the TLRV computed for two slips using the two different methods for treating edge-effect. To provide a further comparison with Yamamura's treatment, the LIM model was assumed to comprise a continuous primary iron. The Bolton correction was applied to the Mosebach results by setting $\sigma^* = \sigma$, and replacing the secondary conductivity by $(K_1/K_2 \cdot \sigma)$, taking care to correct the final results for the reduced primary current density using the K_1 factor as described above. Both methods yield almost the same thrust value at s = .0928 but give somewhat poorer agreement at s = 1.0. This is not surprising since the edge-effect correction is greater at high slip-frequencies and large values of slip. For comparison, the thrust and airgap power computed with the Yamamura theory is given in Table 3. It is interesting that the Yamamura results tend to lie midway between those computed via the Mosebach theory using the two methods for correcting edge-effect. The exception to this is the thrust computed for slip of 0.0928.

TABLE 3. TLRV THRUST AND AIRGAP POWER COMPUTED USING THE MOSEBACH AND BOLTON METHODS FOR EDGE-EFFECT CORRECTION (Included in table are results obtained using Yamamura theory with Bolton methods for edge-effect correction)

	Edge Correction	Thrust (n/side)		Airgap Power (KW/side)	
		Mosebach	Yamamura	Mosebach	Yamamura
s=.0928	Mosebach: Eq'n 46	3398	-	674	-
	Bolton: K_1, K_2	3380	3621	600	634
s=1.0	Mosebach: Eq'n 46	1201		183	
	Bolton: K_1, K_2	1421	1299	208	195

2.3.3 Further Boundary-Effect Considerations

LIM characteristics are altered in varying amounts by the finite size of the primary winding and primary iron core structure. In this section, the cumulative effects of finite primary current winding and finite primary iron core on the TLRV thrust-versus-slip characteristics are examined.

Four different LIM models were considered for this purpose having boundary limiting characteristics as shown below. Model A corresponds to an 'ideal' LIM having no boundary limitations, while Model D describes a LIM having finite primary winding and finite length of iron core. Models B and C describe configurations with boundary limitations intermediate between those of Model A and D.

Model	Primary Winding	Primary Ferromagnetic Region
A	Infinite in x,z plane	Infinite in x,z plane
B	Finite in x-dir. Infinite in z-dir.	Infinite in x,z plane
C	Finite in x-dir. Finite in z-dir.	Infinite in x,z plane
D	Finite in x-dir. Finite in z-dir.	Finite in x-direction Infinite in z-direction

The LIM thrust computed as a function of motor slip is shown in Figure 12 for the different models. In the absence of boundary limitation effects, Model A predicts a peak thrust approaching 51 kilonewtons at a slip near 0.01. The finite length of primary winding (Model B) mainly causes a reduction in thrust at slips below 0.2. Limiting the width of the primary winding (Model C) results in a large increase in thrust over the full range of slips, while the addition of finite ferromagnetic primary (Model D) reduced thrust at slips below 0.2, in a manner not dissimilar to that produced by the finite length of primary winding.

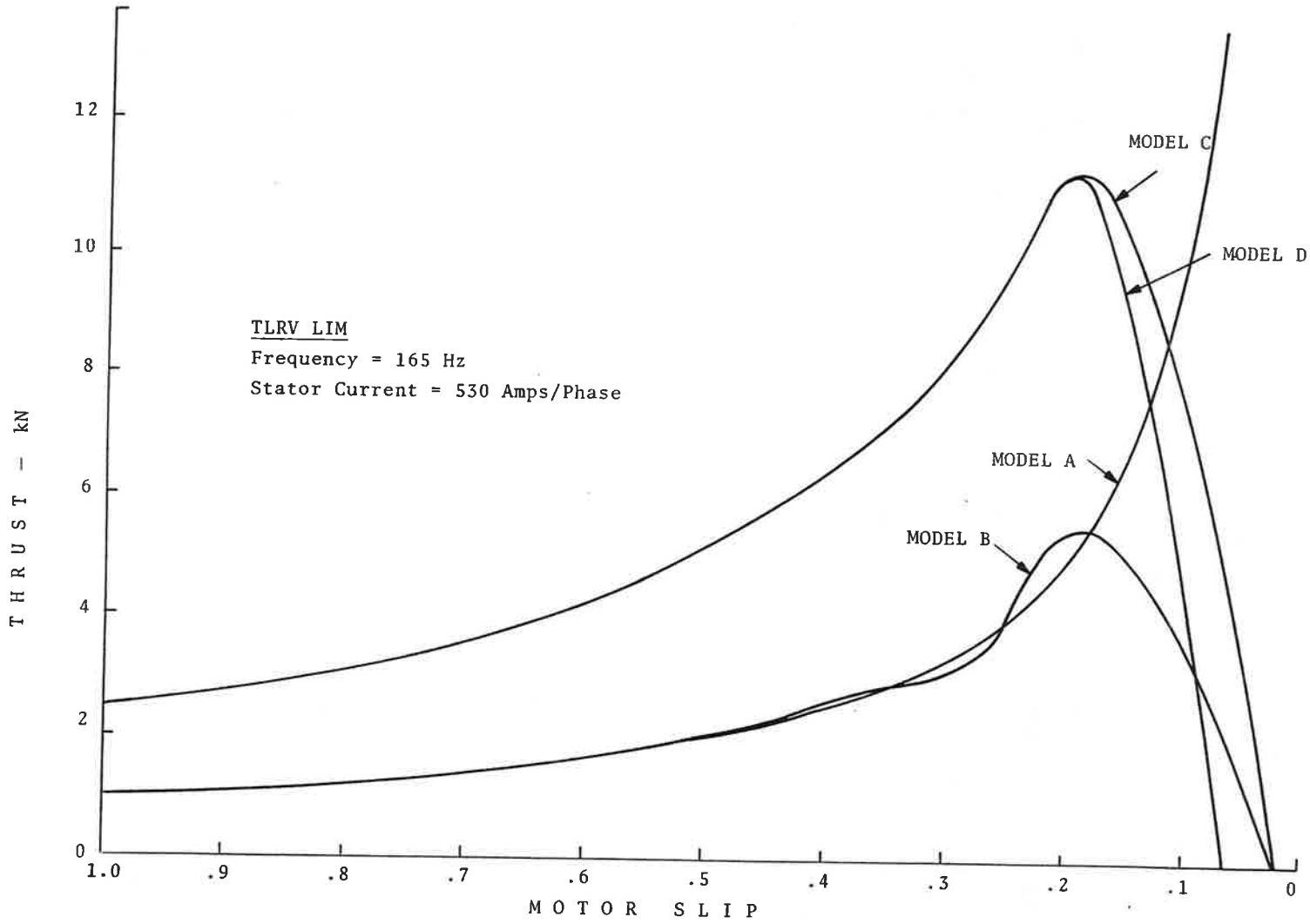

Figure 12. Thrust Predicted for TLRV LIM by Mosebach Theory for Different Boundary Perturbations

2.4 COMPUTER STUDIES OF TLRV & LIMRV LIMS

This section considers the thrust prediction based on the Mosebach model and compares them with results supplied by Dr. D. Elliott and computer predictions based on the Oberretl and Yamamura LIM models. The latter computer predictions were obtained using computer programs described in the first two reports[2,3] in this series.

The LIM parameters describing the TLRV and LIMRV motors are given in Tables 4 and 5. The value of primary core separation (airgap) and secondary thickness includes corrections for the Carter factor and the structural (web-like) characteristics of the secondary. The widths of the secondaries are adjusted to compensate for asymmetrical positioning of the secondaries relative to the primaries, using the theory of Bolton.[7] The same values of LIM parameters are used in the computer studies in order to provide a consistent basis for comparing the computer results.

2.4.1 TLRV LIM Thrust at Rated Speed

The TLRV thrust versus stator excitation frequency is shown in Figure 13 for four different LIM models. Above 185 Hz, the Mosebach, Oberretl, and Yamamura models give predicted thrusts which are in fair agreement, with the maximum divergence in predicted thrust amounting to ten percent. Below 185 Hz, the Mosebach prediction drops off sharply as a result of the finite length of the primary iron core. A similar decrease in the Elliott thrust is also observed, though at the lowest frequency considered (165 Hz), the Elliott model predicts greater thrust than does the Mosebach model.

2.4.2 LIMRV LIM Thrust at Rated Speed

The LIMRV thrust versus stator excitation frequency is shown in Figure 14 for four different LIM models. The agreement in the thrust predictions is reasonably good, both in terms of absolute thrust and general shape of thrust characteristic. Omitting the Yamamura prediction at frequencies below 175 Hz considerably improves the overall thrust agreement. In this case, thrust

TABLE 4. TLRV LIM PARAMETERS

Turns per Coil	(N)	=	4
Pole Pitch	(τ_p)	=	0.448 m.
Core Width	(2c)	=	0.1905 m.
Poles	(P)	=	5
Core Length	(ℓ_s)	=	2.56 m.
Air Gap	(g)	=	0.0171 m.
Phases	(m)	=	3
Slot per Phase	(q)	=	5
End Half-filled Slots	(ε)	=	5
Secondary Thickness	(b)	=	.0066 m.
Secondary Resistivity	(ρ)	=	$.416 \times 10^{-7}$ ohm-m.

TABLE 5. LIMRV LIM PARAMETERS

Turns per Coil	(N)	=	1
Pole Pitch	(τ_p)	=	.355 m.
Core Width	(2c)	=	.254 m.
Poles	(P)	=	10
Core Length	(ℓ_s)	=	3.81 m.
Air Gap	(g)	=	.024 m.
Phases	(m)	=	3
Slots per Phase	(q)	=	5
End Half-filled Slots	(ε)	=	5
Secondary Thickness	(b)	=	.0071 m.
Secondary Resistivity	(ρ)	=	0.416×10^{-7} ohm-m.

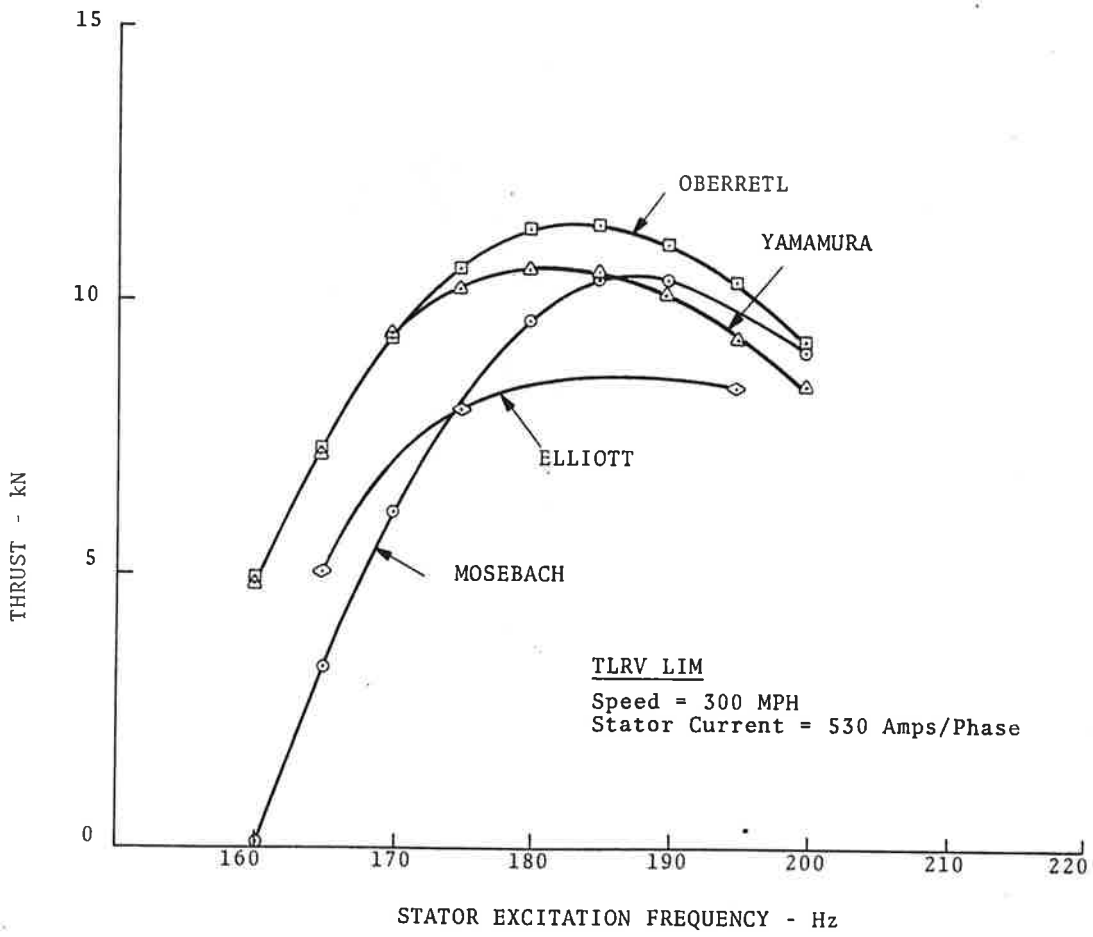

Figure 13. TLRV LIM Thrust as Predicted by Four Leading Theories

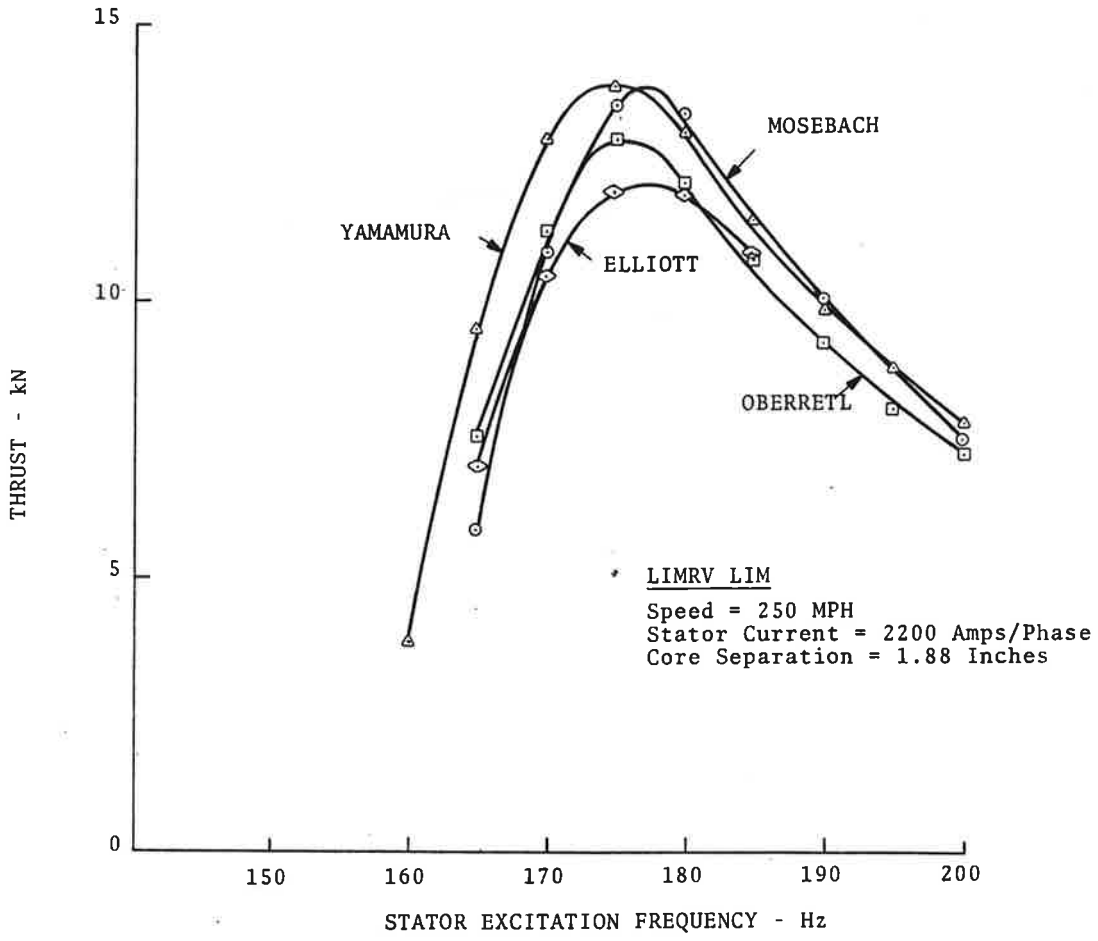

Figure 14. LIMRV LIM Thrust as Predicted by Four Leading Theories

deviations amount to 0.5 kN at 200 Hz and 1.7 kN at 165 Hz, or percent deviations of 7 and 22 percent respectively.

The comparison of the Mosebach, Elliott thrust curves which include magnetic end-effects, with the Oberretl, Yamamura thrust curves which neglect magnetic end-effects, shows little evidence of any appreciable magnetic end-effects in the motor characteristics. Only at the lowest frequency considered, namely 165 Hz, does the Mosebach (and Elliott) curve fall below the thrust predictions of Oberretl and Yamamura. This is in sharp contrast to the thrust results for the TLRV LIM given in Figure 14 which show magnetic end-effects becoming an important factor at frequencies even above the frequency of peak LIM thrust. This points up important differences in the high-speed behavior of the LIMRV and TLRV motors; namely, the comparative insensitivity of the LIMRV motor to magnetic end-effects and the models used to describe its performance.

2.4.3 LIMRV Thrust at 5, 40, 80, and 112 M/S

The peak thrust developed by the LIMRV at four different motor speeds was computed and used to predict the maximum thrust capability of the LIMRV over the full range of motor speeds. The peak thrust at a given motor speed was determined by computing the thrust-versus-speed characteristic in the region of peak LIM thrust The input motor phase current was set at 2200 amps/per phase, or 1100 amps/per phase per core side, corresponding to the maximum current for continuous operation of the LIM.

Figures 15-18 show LIMRV thrust-versus-frequency computed at motor speeds of 5, 40, 80, and 112 M/S. The thrust predicted by the Mosebach one-dimensional model is shown along with the comparative predictions based on the Oberretl and Yamamura models.

The locus of peak thrust is shown plotted in Figure 19 for the Mosebach, Oberretl, Yamamura, and Elliott models. Data for the Elliott model was kindly supplied by Dr. D. Elliott. The decrease in peak thrust with increasing motor speed is due primarily to the MMF end-effect. In the limit of zero motor speed (locked-motor),

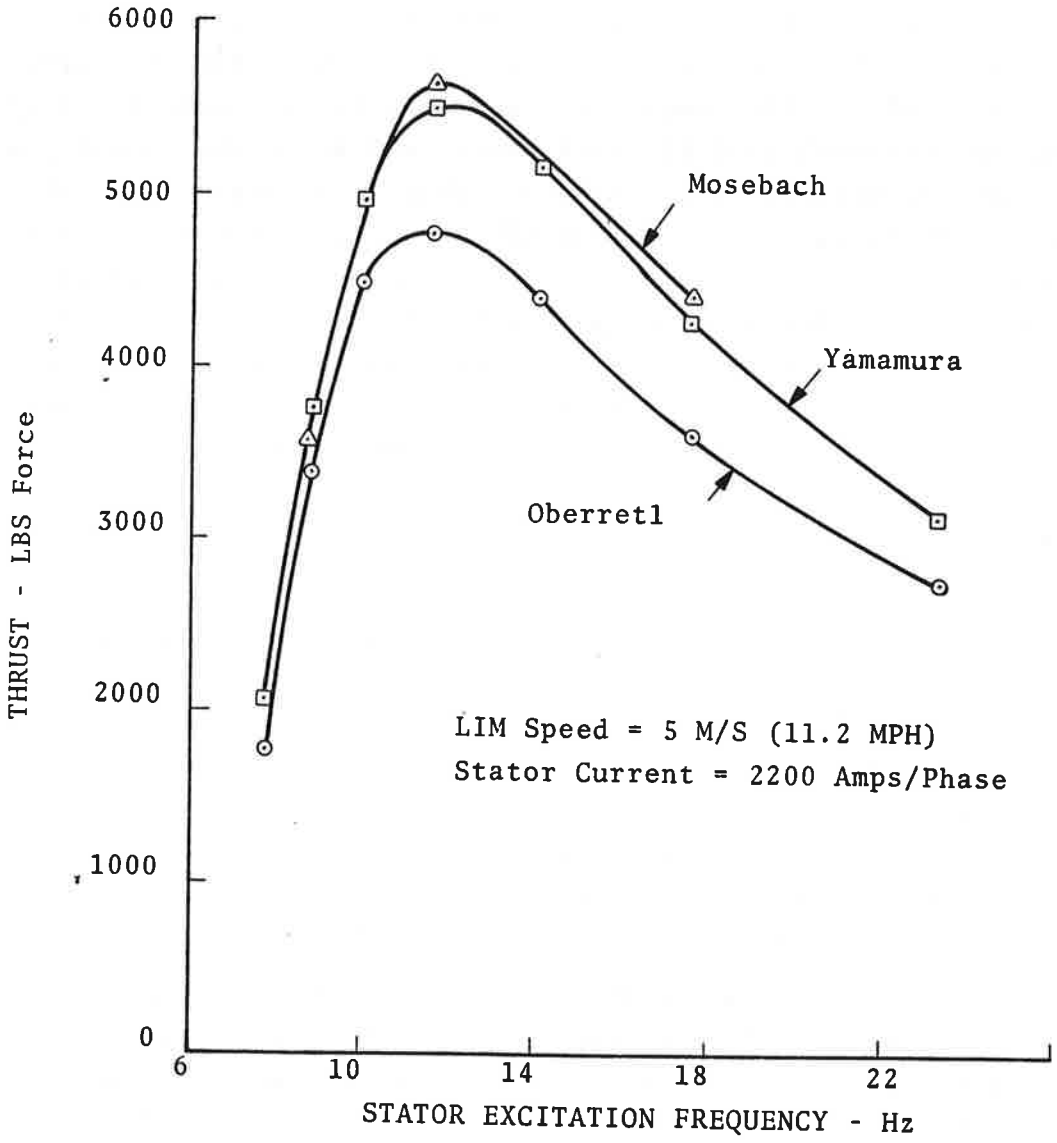

Figure 15. LIMRV Thrust at 5 M/S as Predicted by Three Leading Theories

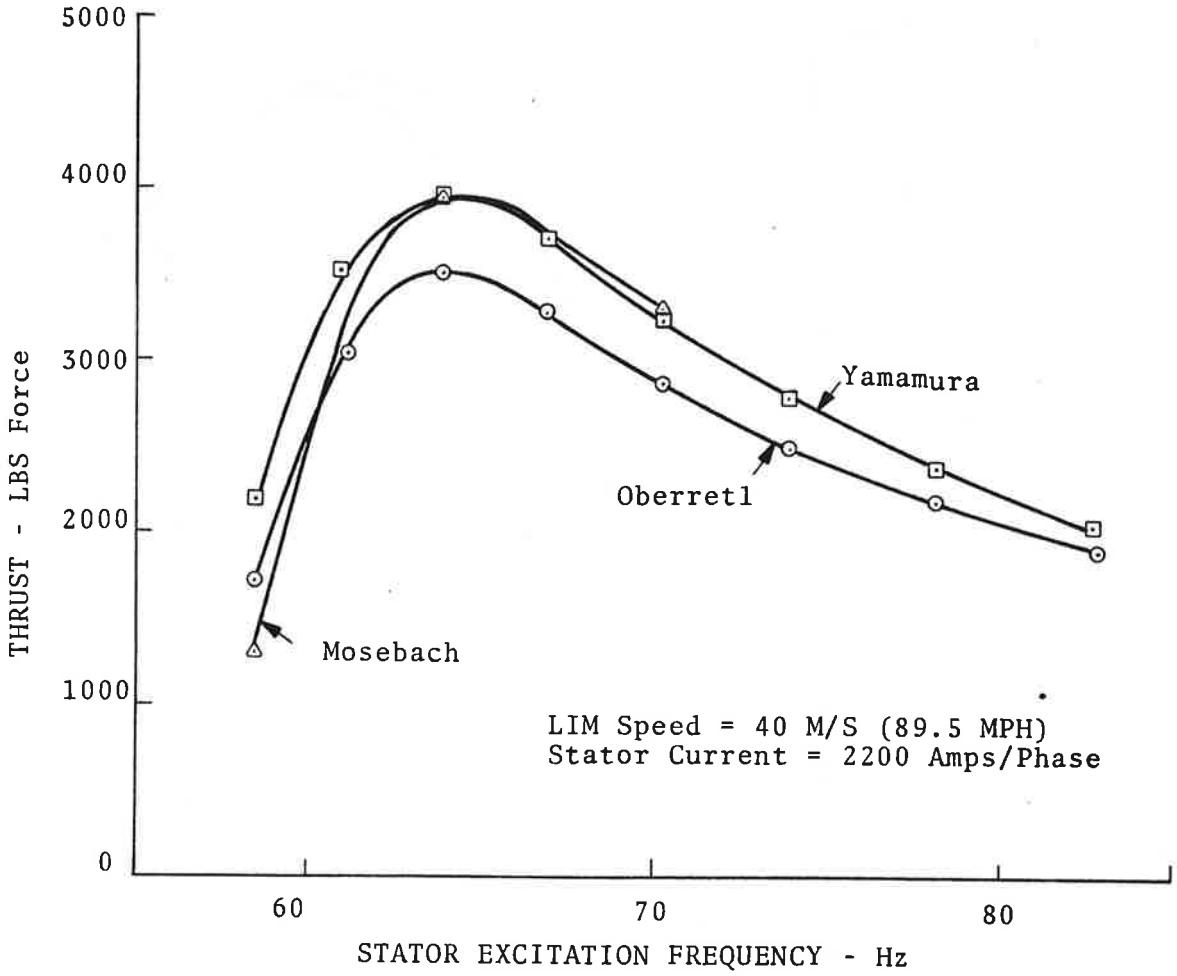

Figure 16. LIMRV Thrust at 40 M/S as Predicted by Three Leading Theories

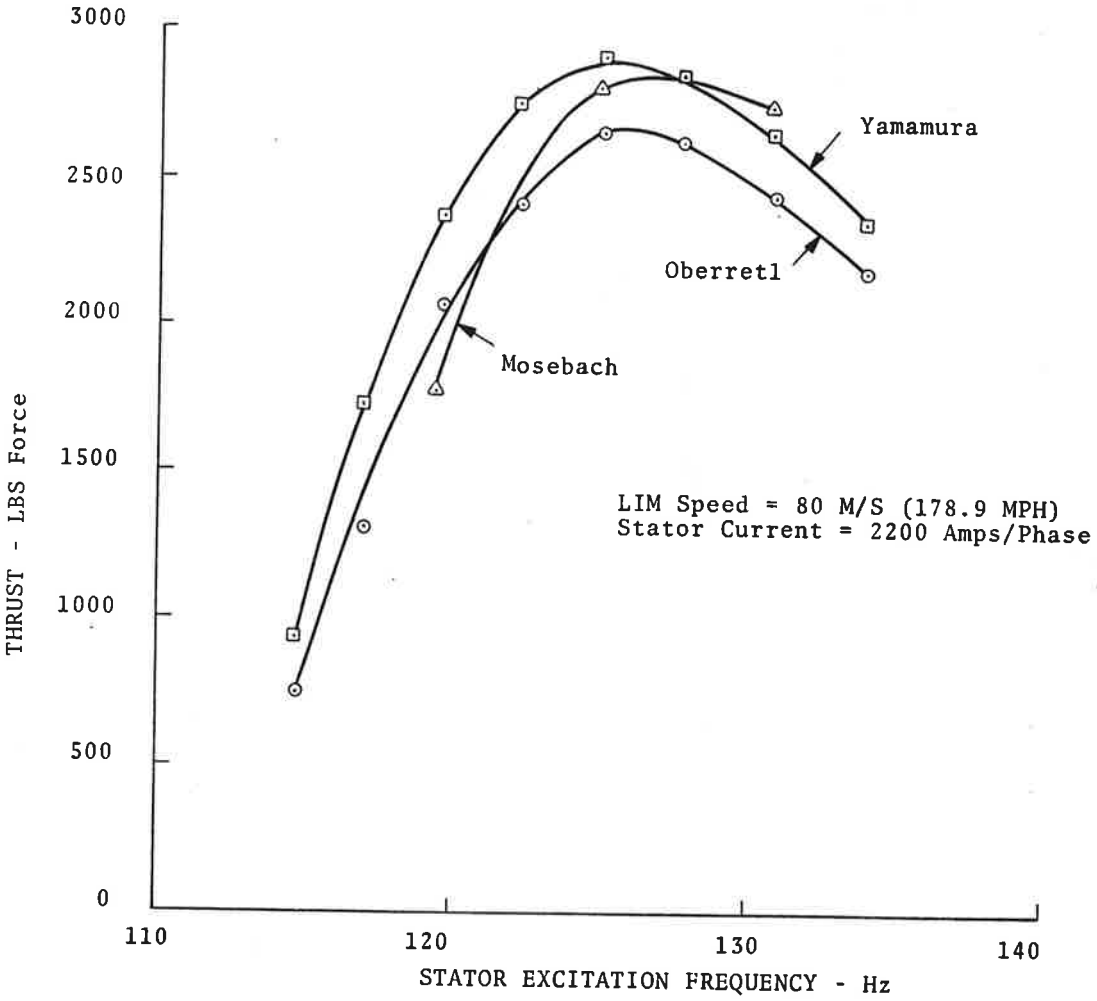

Figure 17. LIMRV Thrust at 80 M/S as Predicted by Three Leading Theories

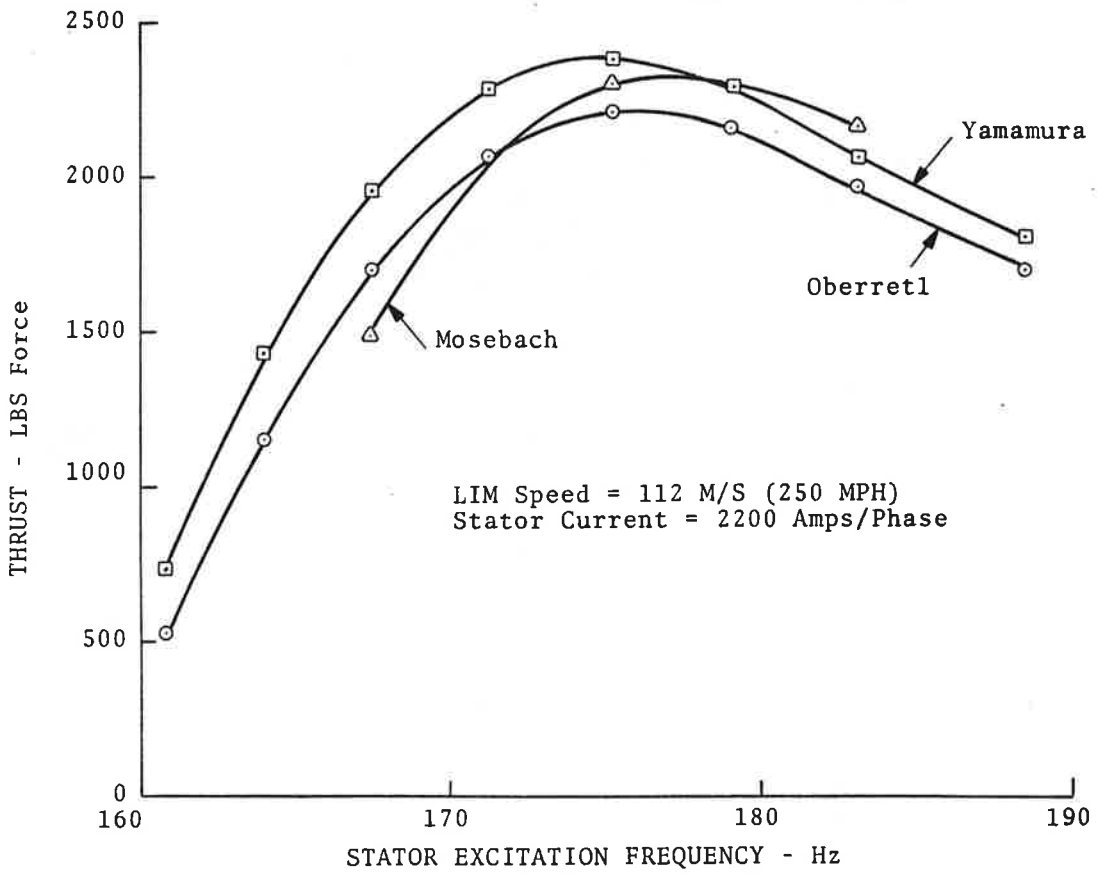

Figure 18. LIMRV Thrust at 112 M/S as Predicted by Three Leading Theories

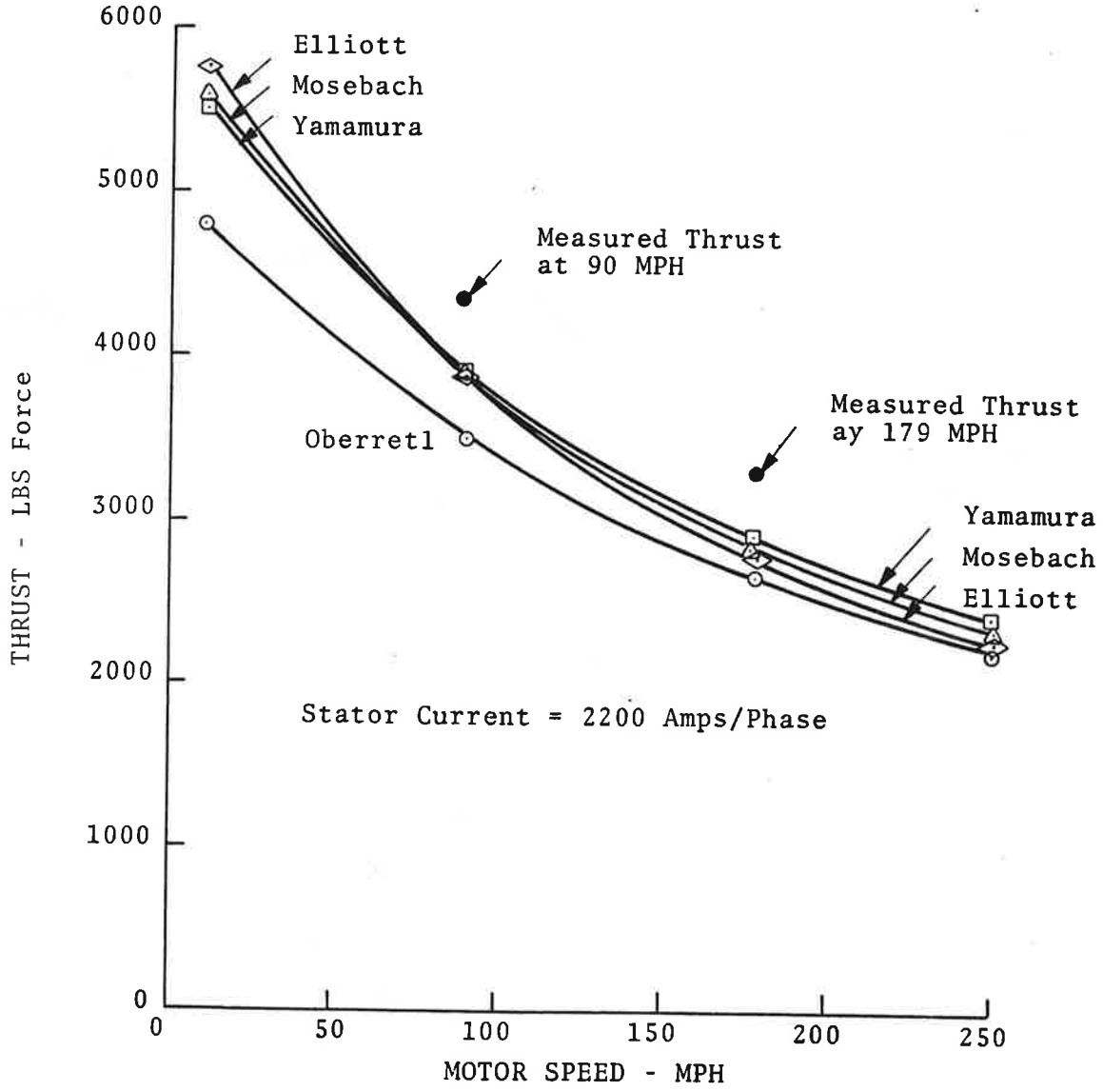

Figure 19. Maximum LIMRV Thrust that can be Developed at Various Speeds as Predicted by Four Leading Theories

end-effects become unimportant and the peak thrust should approach that of a rotary motor with equivalent primary current excitation.

The measured thrust at 90 and 179 MPH obtained from test runs at Pueblo, Colorado (Test Run No. 105-4) are indicated in the figure. The data points were adjusted for an average stator current of 2200 amps/phase. The measured thrust tends to exceed the predicted thrusts by about 400-450 pounds. The theoretical thrust curves shown in Figure 19 were computed on a constant input current basis. Later calculations using the Mosebach computer program on a constant input voltage basis yielded considerably better agreement at higher motor speeds. These latter results are presented in Section 2.5.2.

2.4.4 LIMRV LIM Equivalent Circuit

The equivalent circuit parameters for the LIMRV motor are examined in this section using the Mosebach theory together with empirical data obtained from test runs at Pueblo, Colorado. Figure 20 shows the equivalent LIM circuit and characteristic impedance parameters. The input impedance of the motor (Z_{in}) is equal to the air-gap impedance (Z_{ag}) plus the series winding resistance and leakage reactance.

$$Z_{in} = R_1 + jX_i + Z_{ag} \tag{47}$$

The input impedance (per phase) is determined from the measured voltage, current ratio (per phase) and the measured power factor angle θ.

$$Z_{in} = (V/I)\underline{/\theta} \tag{48}$$

The air-gap impedance is computed from the Mosebach theory as equal to the voltage induced in the phase winding when currents of one ampere flow through each of the phase windings. From Equation (47),

$$R_1 + jX_1 = Z_{in} - Z_{ag} \tag{49}$$

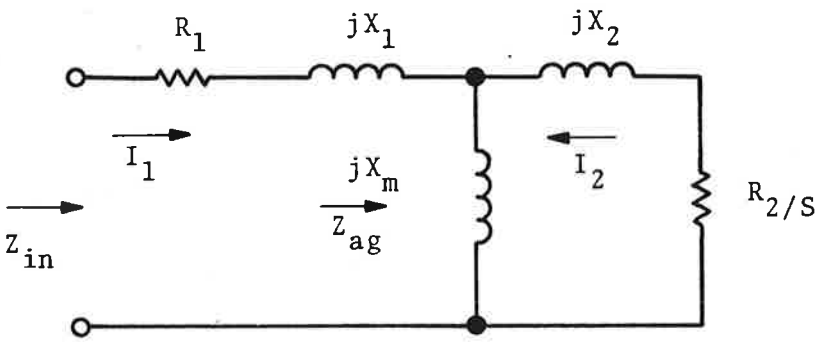

Figure 20. LIM Equivalent Circuit

The magnetizing reactance (jX_m) is found from the air-gap impedance evaluated for zero secondary conductivity.

$$Z_{ag}^{(o)} = jX_m \tag{50}$$

It then follows that the secondary impedance parameters R_2, X_2, are determined from,

$$R_2 + jX_2 = \frac{1}{\frac{1}{Z_{ag}} - \frac{1}{Z_{ag}^{(o)}}} \tag{51}$$

The Mosebach theory predicts that R_2 and X_2 will vary with slip frequency, R_2 increasing with slip frequency and the ratio X_2/X_m decreasing with slip frequency. The above functional dependences are expected since the secondary current flow lines are forced to alter their paths due to the large impeding fluxes set up by the longitudinal currents at increased slip frequencies.[5] The result is a constriction of current flow in the secondary and a shift in the x-directed secondary currents away from the active region of the motor which leads to an increase in secondary resistance and decrease in secondary leakage inductance, respectively.

The equivalent circuit parameters for the LIMRV motor were computed using the Mosebach one-dimensional computer program together with data obtained from test runs of the LIMRV at Pueblo, Colorado. The circuit parameters were evaluated at five motor speeds chosen at approximately 40 MPH intervals. Table 6 lists the values of equivalent circuit parameters for each motor speed. The increase in AC resistance of the primary winding (R_1) is as expected due to the eddy current effect at higher frequencies. L_2 decreases with frequency and R_2 exhibits a slight increase with frequency as predicted above. The values given in the table represent average values for all three phase windings.

The predicted LIM thrust is compared with measured thrust in Table 7 using the Mosebach computer program and assuming constant voltage excitation of the primary. The agreement at high frequencies is excellent, but tends to fall off as the frequency is reduced. At the lowest frequency (and speed) the percent deviation is slightly under ten percent.

TABLE 6. LIMRV EQUIVALENT CIRCUIT PARAMETERS COMPUTED USING MOSEBACH THEORY

LIM SPEED (MPH)	FREQ (HZ)	SLIP	R_1 (OHM)	L_1 (MH)	L_m (MH)	R_2 (OHM)	L_2 (MH)
20	17.2	.269	.0161	.203	.843	.0294	.116
60	45.5	.173	.0267	.221	.843	.0283	.111
100	72.9	.138	.0309	.245	.843	.0285	.114
140	101.1	.130	.0361	.224	.843	.0291	.095
178	127.9	.125	.0400	.235	.843	.0296	.084

TABLE 7. COMPARISON OF MEASURED AND PREDICTED LIMRV THRUST

LIM SPEED (MPH)	FREQ (HZ)	MEASURED THRUST* (LBS)	COMPUTED THRUST* (LBS)	DEVIATION (PERCENT)
20	17.2	2903	2621	-9.7
60	45.5	3661	3352	-8.4
100	72.9	3505	3286	-6.2
140	101.1	3468	3356	-3.2
178	127.9	3214	3166	-1.5

*Thrust for one core side

3. CONCLUSIONS

The Mosebach theory of double-sided linear induction motors has been reviewed and used to predict LIM characteristics of two high-speed motors (TLRV & LIMRV LIM's). The effects of finite iron core and primary MMF excitation on LIM performance are examined using the one-dimensional version of the Mosebach theory. The LIM characteristics predicted by the Mosebach theory are compared with predictions given by theories developed by K. Oberretl, S. Yamamura, and D. Elliott.

Magnetic end-effects caused by the finite length of primary core are shown to degrade LIM performance under conditions of high motor speed and low slip. This phenomena has certain characteristics similar to those associated with the MMF end-effect, high motor speed, and low slip. Under such conditions the total real power delivered to the motor remains constant but the fraction converted in usable mechanical power is reduced. This is reflected in a drop in motor efficiency at high speeds. For the TLRV operating at rated speed (300 MPH) and a slip of about 1/10, theory predicts a drop in motor efficiency from 77 to 33 percent due to magnetic end-effects.

The method of treating MMF edge-effect in the Mosebach theory is examined and compared with the Bolton treatment as applied in the Yamamura LIM theory. Both methods use approximations required to make the solutions tractable. In the Mosebach approach, these approximations take the form of severe restrictions in the flow pattern of the secondary currents and the neglect of the transverse functional dependence of the air-gap flux density (one-dimensional model). In the Bolton approach, the secondary current is restricted only to flow in the plane of the secondary (eddy currents neglected). The correction for the edge-effect is derived for the condition of no MMF end-effects. Since end-effects and edge-effects are coupled phenomena, the neglect of cross-coupling between the two boundary effects leads to errors when both effects become important. Studies of the effect of different boundary perturbations on TLRV

LIM performance show that MMF edge-effect is an important factor in thrust development at all motor slips.

The TLRV and LIMRV thrust-versus-frequency characteristics were computed for rated motor speeds using the Mosebach (one-dimensional) computer program and compared with similar studies using the Oberretl, Yamamura, and Elliott computer programs. (Results of Elliott computer studies are kindly supplied by Dr. D. Elliott.) At high slip-frequencies, the computed thrusts were in reasonably agreement, with maximum spread in thrust values amounting to less than ten percent. At low slip frequencies where magnetic end-effects were important, the Mosebach and Elliott thrust values were lower than those of Oberettl and Yamamura. Magnetic end-effects were observed to be considerably more pronounced in the TLRV LIM than in the LIMRV LIM, a result due to the characteristicly higher speed of the TLRV LIM.

Constant input voltage calculations were made for the LIMRV LIM at five different motor speeds. The computed Mosebach thrusts were compared with thrust data obtained from test runs at Pueblo, Colorado. At speeds of 140 and 178 MPH, the predicted thrusts were within three percent of measured thrusts and at low speeds, within ten percent of measured thrusts. Similar calculations performed on a constant input <u>current</u> basis gave somewhat poorer agreement at the higher motor speeds than those on a constant <u>voltage</u> basis.

The equivalent circuit parameters of the LIMRV LIM were computed using the Mosebach theory and empirical data obtained from test runs at Pueblo, Colordao. All circuit parameters except the magnetizing inductance vary with frequency (and motor speed). The primary series resistance increases with frequency due to eddy currents. The increase in secondary resistance and decrease in secondary leakage inductance with frequency is attributed to the change in secondary current paths required to accommodate the increased reactive impedance in the secondary circuit.

The method used by Mosebach to include finite iron primary in the LIM model using an effective air-gap function requires further

study. In certain instances, the amplitudes of the air-gap harmonics can be comparable with pole pitch and thereby violate a basic assumption used in formulating the LIM model. The error introduced by this process could be important and should be examined in applications requiring accurate results.

The computer time needed for a given run is a function of the primary winding and the harmonics necessary to describe the field and current distributions of the motor. Substantial savings in computer time might be realized if fewer Fourier harmonics were utilized in the numerical calculations. Restricting the maximum harmonic order to 2.5-3.0 times the harmonic order of the fundamental would probably be sufficient for most computations. The reduction in the number of positive harmonic orders used in the field expansion should be considered since they contribute very little to the ultimate answer.

4. REFERENCES

1. Mosebach, H., "Effekte der endlichen Länge und Breite bei asynchronen Linearmotoren in Kurzständer- und Kurzläufer-bauform," Dissertation Technische Universität Braunschweig 1972.

2. Stickler, J., "A Study of Linear Induction Motor Characteristics: The Oberretl Model," Transportation Systems Center, Cambridge MA, DOT-TSC-FRA-75-2/FRA-OR&D-75-72, May 1975.

3. Stickler, J., "Evaluation of Linear Induction Motor Characteristics: The Yamamura Model," Transportation Systems Center, Cambridge MA, DOT-TSC-FRA-75-1/FRA-OR&D-75-40, April 1975.

4. Weh, H., Waltke, G., and Appun, P., "Induction Phenomena in MHD Converters with Constant and Traveling Magnetic Field," Energy Conversion 9, (1), 31-38 (March 1969).

5. Bolton, H., "Transverse Edge-Effect in Sheet-Rotor Induction Motors," Proc. IEE, 116, (5), 725-731, May 1969.

6. Yamamura, S., Theory of Linear Induction Motors, John Wiley & Sons, New York, NY, 1972, Appendix 1.

7. Bolton, H., "Forces in Induction Motors with Laterally Asymmetric Sheet Secondaries," Proc. IEE, 117, (12), 2241-2248, December 1970.